

RELAXED GAUSS–NEWTON METHODS WITH APPLICATIONS TO ELECTRICAL IMPEDANCE TOMOGRAPHY

Jyrki Jauhainen* Petri Kuusela* Aku Seppänen* Tuomo Valkonen†

2020–05–13

Abstract As second-order methods, Gauss–Newton-type methods can be more effective than first-order methods for the solution of nonsmooth optimization problems with expensive-to-evaluate smooth components. Such methods, however, often do not converge. Motivated by nonlinear inverse problems with nonsmooth regularization, we propose a new Gauss–Newton-type method with inexact relaxed steps. We prove that the method converges to a set of disjoint critical points given that the linearisation of the forward operator for the inverse problem is sufficiently precise. We extensively evaluate the performance of the method on electrical impedance tomography (EIT).

1 INTRODUCTION

The classical Gauss–Newton method can be used for the iterative solution of nonlinear least squares problems $\min_x \frac{1}{2} \|A(x)\|^2$. It works by successive linearisation of the nonlinear operator $A \in C^1(V; \mathbb{R}^M)$ defined on $V \subset \mathbb{R}^n$. Often, not the least in inverse problems and data science, one wishes to combine such a least squares fitting with a nonsmooth but convex regularization term $F : V \rightarrow \mathbb{R}$ incorporating prior information of a good approximate solution to the ill-posed problem $A(x) = 0$. We thus wish to solve

$$(1.1) \quad \min_x J(x) := \frac{1}{2} \|A(x)\|^2 + F(x).$$

One readily extends the idea behind the Gauss–Newton method to this problem: linearise A , solve the resulting convex nonsmooth problem to high accuracy, repeat. Unfortunately, such a basic approach rarely converges, especially in inverse problems where A and its differentials almost by definition are not injective. In this work, after several relaxations of the approach, we prove the convergence of a variant of the Gauss–Newton method for (1.1), concentrating on applications to electrical impedance tomography (EIT).

*Department Of Applied Physics, University of Eastern Finland, Kuopio, Finland. jyrki.jauhainen@uef.fi

†ModeMat, Escuela Politécnica Nacional, Quito, Ecuador *and* Department of Mathematics and Statistics, University of Helsinki, Finland. tuomo.valkonen@iki.fi

NONSMOOTH NONCONVEX OPTIMIZATION METHODS

If F and A are sufficiently smooth, (1.1) can frequently be solved with Newton’s method. A small degree of nonsmoothness can be dealt with semismooth Newton’s method [31, 36, 37]. If F is nonsmooth, nonlinear primal-dual proximal splitting (NL-PDPS) [44, 12] is one possibility; see [47] for an overview. Usually NL-PDPS as a first-order method requires thousands of iterations to converge. If the iterations are computationally costly, the method becomes impractical. This can be the case for A the solution operator of a partial differential equation (PDE). We are thus led to Gauss–Newton-type methods that combine both worlds, however, they often fail to converge [44].

Convergence analysis of the classical Gauss–Newton, for the nonlinear least squares problem $\min_x \frac{1}{2} \|T(x)\|^2$, with T Lipschitz-continuously differentiable, may be found, for example, in [33]. In [34] merely locally Lipschitz T is considered. Several works have also studied extensions of the Gauss–Newton method to the general composite minimization problem $\min_x h(T(x))$; see, for example, [7, 15, 27]. These works generally assume that the set of minima C of h is “weakly sharp”, and that the inclusion $T(x) \in C$ has some “regular points”. In our setting, writing $h(x, y) = G(x) + F(y)$ for $T(x) = (A(x), x)$, the existence of a “regular point” would reduce to the injectivity of the differential $A'(\hat{x})$ at a minimiser \hat{x} of J . Since, in inverse problems, the range of A is generally much smaller than the domain, such a condition cannot be expected to hold. The assumption of “weak sharp minima” amounts to strong metric subregularity of the objective at the solution set. According to [1], this is a local form of strong convexity.

In [40] the Gauss–Newton method is studied for problems of the specific form (1.1). There also, $A'(\hat{x})$ has to be injective, and the sub-problem solutions exact. In this case, linear convergence is proved. However, we want to avoid such injectivity assumptions, and also allow the sub-problems to be solved inexactly. To be able to do this, and still obtain convergence, *we will introduce a relaxation term into our subproblems, and relaxation step between the Gauss–Newtons steps*. The former connects our approach to the classical Levenberg–Marquardt method which, indeed, can be seen as a proximal Gauss–Newton method for nonlinear least squares [22, 19]. *We also will not require the sub-problems to be solved exactly*, merely to obtain sufficient decrease following a condition akin to what has been employed in a different context in [6, 3]. With this, in Section 2, we will show the convergence of iterates of the proposed *Relaxed Inexact Proximal Gauss–Newton* method (RIPGN) to *disjoint components* of critical points. In particular, if the critical points are isolated, we will obtain convergence.

ELECTRICAL IMPEDANCE TOMOGRAPHY

We will evaluate the proposed method on image (conductivity) reconstruction in Electrical Impedance Tomography (EIT). This is a large-scale nonlinear PDE-constrained inverse problem. EIT is an imaging technique in which electric conductivity in a target domain is reconstructed from boundary measurements. The relationship between the boundary measurements and the electrical potential and conductivity within the domain are governed by a nonlinear elliptic partial differential equation. In general, the underlying inverse problem of EIT, which is also known as Calderon’s problem [8], is ill-posed in the sense that it doesn’t depend continuously on the boundary data. However, by assuming certain bounds on the conductivity, it is possible to

show an optimal logarithmic modulus of continuity [39]. This, of course, means that even small changes in the conductivity can cause large changes in the boundary values. Cases of nonsmooth conductivities in two dimensions are considered in paper [2]. For cases of piecewise analytic and smooth conductivities in three dimensions, we refer to [23, 24] and [42], respectively.

Theoretical work on the inverse problem of EIT has introduced several direct methods for reconstructing the conductivity. In recent years, so-called D-bar method, which utilizes complex geometrical optics solutions to the Schrödinger formulation of the inverse conductivity problem, has undergone considerable progress [43, 32]. In the present, however, we formulate the inverse conductivity problem as a least squares minimization problem between the boundary values from the PDE and measurement data. Optimization and Tikhonov-regularization based approach offers several benefits over the direct methods. It is easier to include physically more accurate boundary conditions, domain shapes and regularization functions. Moreover, in a Bayesian framework, the optimization-based solution can be considered as maximum a posteriori estimates with certain prior distribution [21]. With further analysis, error estimates may also be obtained [4]. The underlying optimization problem is, however, often tricky to solve, as the boundary currents depend nonlinearly on the conductivity. This means that the optimization problem is nonconvex. Moreover, total variation type regularization, which help to reconstruct the boundaries of different materials within the target domain, makes the problem nonsmooth.

ORGANIZATION

The rest of this paper is organized as follows: first, in [Section 2](#), we examine the convergence of the relaxed inexact proximal Gauss–Newton method. For a certain relaxation parameter, we show that the algorithm converges to a disjoint set of Clarke critical points, given that the linearisation of the operator A sufficiently well approximates the original operator. In [Section 3](#), we provide a more detailed description of the algorithm and explain how to reliably solve linearised nonsmooth subproblems in the Gauss–Newton scheme. In [Sections 4](#) and [5](#), by using EIT as an example, we study numerically and experimentally whether the relaxed Gauss–Newton method improves the computational efficiency of the image reconstructions compared to alternative optimization methods. In these studies, we utilize sythetic data from a water tank setup and experimental measurement data from so-called EIT based sensing skin setup. This is a system for detecting surface changes, eg. cracks, on the given target[18]. In [Appendices B](#) and [C](#) we provide further reconstructions for these setups and their variants.

2 CONVERGENCE PROPERTIES OF THE RELAXED INEXACT PROXIMAL GAUSS–NEWTON METHOD

We intend to solve problem (1.1) by successive linearisations of A : for some z^k we take

$$A_k(x) := \tilde{A}_{z^k}(x) \quad \text{with} \quad \tilde{A}_y(x) := A(y) + \nabla A(y)^*(x - y)$$

Algorithm 2.1 Outline of relaxed inexact proximal Gauss–Newton method (RIPGN).

Require: Convex, proper, lower semicontinuous $F : \mathbb{R}^N \rightarrow \overline{\mathbb{R}}$ and $A \in C^1(\text{dom } F; \mathbb{R}^M)$.

Require: Relaxation parameter $w > 0$.

- 1: Choose an initial iterate $z^0 \in \text{dom } F$.
 - 2: **for all** $k \geq 0$ **do**
 - 3: Find an approximate solution \tilde{x}^k to (2.2).
 - 4: Update $z^{k+1} := (1 - w)z^k + w\tilde{x}^k$
 - 5: **end for**
-

A standard Gauss–Newton-type approach would then solve on each iteration the linearised, convex problem

$$(2.1) \quad \min_x J_k(x) := \frac{1}{2} \|A_k(x)\|^2 + F(x)$$

and update $z^{k+1} := \tilde{x}^k$ to form the linearisation point of the next iteration. As we have remarked in the introduction, such a method seldom converges. Our plan, to obtain a convergent method, is to solve for some *proximal parameter* $\beta > 0$ the modified problem

$$(2.2) \quad \min_x \tilde{J}_k(x) := \frac{1}{2} \|A_k(x)\|^2 + F(x) + \frac{\beta}{2} \|x - z^k\|^2 = J_k(x) + \frac{\beta}{2} \|x - z^k\|^2.$$

Then we take the linearisation point z^{k+1} as an interpolation between \tilde{x}^k and z^k , precisely

$$z^{k+1} := (1 - w)z^k + w\tilde{x}^k$$

for a sufficiently small *relaxation parameter* $w \in (0, 1]$. Furthermore, we allow \tilde{x}^k to be solved inexactly from (2.2). This yields our outline method of [Algorithm 2.1](#), the *relaxed inexact proximal Gauss–Newton* method (RIPGN).

We now prove the convergence of the method with $\beta > 0$. In [Appendix A](#) we show that it is possible to take $\beta = 0$ under strong metric subregularity. We need assumptions that guarantee that the solutions of the linearised subproblems stay in a bounded set, and we need the linearisations \tilde{A}_y to locally approximate A sufficiently well:

Assumption 2.1. $F : \mathbb{R}^N \rightarrow \overline{\mathbb{R}}$ is convex, proper, and lower semicontinuous, the operator $A \in C^1(\text{dom } F; \mathbb{R}^M)$, and

$$J(x) := \frac{1}{2} \|A(x)\|^2 + F(x).$$

Given an initial iterate $z^0 \in \mathbb{R}^N$, the sublevel set $\text{lev}_{J(z^0)} J$ is bounded, $\inf F > -\infty$, and $A_{\max} := \sup_{z \in \text{dom } F} \|A(z)\| < \infty$. Moreover, for some $\mathfrak{d}, C > 0$, the linearization error

$$\|A(x) - \tilde{A}_y(x)\| \leq C \|x - y\|^2 \quad (x \in \text{cl } B(y; \mathfrak{d}), y \in \text{lev}_{J(z^0)} J).$$

Here $B(x, r)$ is the open ball of radius r at x while $\text{cl } B(x, r)$ is its closure. We write $\text{dom } F := \{x \in \mathbb{R}^N \mid F(x) < \infty\}$ for the effective domain of F and $\text{lev}_c J := \{x \in \mathbb{R}^N \mid J(x) \leq c\}$ for the c -sublevel set of J . We will also write $\partial J_k(x)$ for the subdifferential of the convex functions J_k at x , and, moreover, denote by $\partial_C J(x)$ the Clarke subdifferential of the non-convex function J at x , as defined in [11]. We call a point x satisfying $0 \in \partial_C J(x)$ Clarke-critical. Then we have:

Theorem 2.1. *Suppose Assumption 2.1 holds and, for some $\beta, \varepsilon > 0$,*

$$(2.3) \quad 0 < w \leq \min \left\{ 1, \frac{\mathfrak{d}}{\sqrt{2\beta^{-1}(J(z^0) - \inf F)}}, \frac{\beta - \varepsilon}{2CA_{\max}} \right\}.$$

On line 3 of Algorithm 2.1, find an approximate minimiser \tilde{x}^k to (2.2) specifically satisfying

1. *For some $e^k \in \partial\tilde{J}(\tilde{x}^k)$ we have $e^k \rightarrow 0$ as $k \rightarrow \infty$, and*
2. *either $\tilde{J}_k(z^k) \geq \tilde{J}_k(\tilde{x}^k)$ with $\tilde{x}^k \neq z^k$, or $\tilde{x}^k = z^k \in [\partial\tilde{J}_k]^{-1}(0)$.*

Then the iterates satisfy:

- (i) *$J(z^k)$ is monotonically decreasing; indeed, $J(z^k) \searrow L$ for some $L \in \mathbb{R}$.*
- (ii) *Any accumulation point \hat{x} of $\{z^k\}_{k \in \mathbb{N}}$ is Clarke-critical and satisfies $J(\hat{x}) = L$;*
- (iii) *Indeed, $\text{dist}(z^k, U) \rightarrow 0$ for a disjoint component U of $V_L := \{\hat{x} \in V \mid 0 \in \partial_C J(\hat{x}), J(\hat{x}) = L\}$.*

Proof. Suppose first that $\tilde{x}^k = z^k \in [\partial\tilde{J}_k]^{-1}(0)$ for some $k \in \mathbb{N}$. Since $\partial\tilde{J}_k(z^k) = \partial J_k(z^k) = \partial_C J(z^k)$, we obtain $z^{k+1} = z^k$, so that there is nothing left to prove: the algorithm has converged to a critical point in a finite number of iterations.

So, by assumption, $\tilde{J}_k(z^k) \geq \tilde{J}_k(\tilde{x}^k)$ with $\tilde{x}^k \neq z^k$ for all $k \in \mathbb{N}$. Using (2.2) we now obtain

$$(2.4) \quad J(z^k) - J_k(\tilde{x}^k) = \tilde{J}_k(z^k) - \tilde{J}_k(\tilde{x}^k) + \frac{\beta}{2} \|\tilde{x}^k - z^k\|^2 \geq \frac{\beta}{2} \|\tilde{x}^k - z^k\|^2 > 0.$$

Since $w \leq 1$, from the convexity of J_k we have

$$(2.5) \quad J(z^k) - J_k(z^{k+1}) \geq J(z^k) - ((1-w)J_k(z^k) + wJ_k(\tilde{x}^k)) = w(J(z^k) - J_k(\tilde{x}^k)).$$

Consequently, by (2.4),

$$J(z^k) - J_k(z^{k+1}) \geq \frac{w\beta}{2} \|\tilde{x}^k - z^k\|^2 > 0.$$

Now we show by induction that

$$(2.6) \quad J(z^0) \geq J(z^k) \quad (k \geq 0).$$

As a by-product, we will verify (i), and obtain useful estimates for (ii) and (iii).

Induction base: Obviously $J(z^0) \geq J(z^k)$ holds for $k = 0$.

Induction step: Suppose $J(z^0) \geq J(z^k)$. We show $J(z^0) \geq J(z^{k+1})$. From (2.4) we have

$$J(z^0) - J_k(\tilde{x}^k) \geq J(z^k) - J_k(\tilde{x}^k) \geq \frac{\beta}{2} \|\tilde{x}^k - z^k\|^2.$$

Since $J_k(\tilde{x}^k) \geq \inf F$, we have

$$\|\tilde{x}^k - z^k\| \leq \sqrt{2\beta^{-1}(J(z^0) - \inf F)} := r,$$

and since $w \leq \delta/r$, it follows

$$(2.7) \quad \|z^{k+1} - z^k\| = w\|\tilde{x}^k - z^k\| \leq wB \leq \frac{\mathfrak{d}}{r}r = \mathfrak{d},$$

thus $z^{k+1} \in \text{cl} B(z^k; \mathfrak{d})$. From Assumption 2.1 with $h := z^{k+1} - z^k$,

$$(2.8) \quad \|A(z^{k+1}) - A_k(z^{k+1})\| \leq C\|z^{k+1} - z^k\|^2 \leq C\|h\|^2.$$

Now using (2.8) and the definition of A_{\max} for the inequality in the next estimate, we obtain

$$(2.9) \quad \begin{aligned} \frac{1}{2}\|A_k(z^{k+1})\|^2 - \frac{1}{2}\|A(z^{k+1})\|^2 &= \frac{1}{2}\|A(z^{k+1}) - A_k(z^{k+1})\|^2 \\ &\quad + \langle A_k(z^{k+1}) - A(z^{k+1}), A(z^{k+1}) \rangle \\ &\geq \langle A_k(z^{k+1}) - A(z^{k+1}), A(z^{k+1}) \rangle \geq -CA_{\max}\|h\|^2. \end{aligned}$$

Furthermore, using (2.9),

$$\begin{aligned} J(z^k) - J(z^{k+1}) &= J(z^k) - \frac{1}{2}\|A(z^{k+1})\|^2 - F(z^{k+1}) \\ &\geq J(z^k) - \frac{1}{2}\|A_k(z^{k+1})\|^2 - F(z^{k+1}) - CA_{\max}\|h\|^2 \\ &= J(z^k) - J_k(z^{k+1}) - CA_{\max}\|h\|^2. \end{aligned}$$

Using (2.5), (2.7), and (2.4), we continue

$$\begin{aligned} J(z^k) - J(z^{k+1}) &\geq w(J(z^k) - J_K(\tilde{x}^k)) - CA_{\max}\|h\|^2 \\ &= w(J(z^k) - J_K(\tilde{x}^k)) - \frac{2w^2CA_{\max}\|\tilde{x}^k - z^k\|^2}{2} \\ &\geq w \left(\frac{\beta\|\tilde{x}^k - z^k\|^2 - 2wCA_{\max}\|\tilde{x}^k - z^k\|^2}{2} \right). \end{aligned}$$

Since (2.3) implies $\beta \geq 2wCA_{\max} + \varepsilon$ for some $\varepsilon > 0$, we deduce that

$$J(z^k) - J(z^{k+1}) \geq \frac{w\varepsilon}{2}\|z^k - \tilde{x}^k\|^2 > 0.$$

With this and $J(z^0) \geq J(z^k)$, we get $J(z^0) > J(z^{k+1})$. This completes the proof of the induction step and consequently (2.6).

In the process, we obtained

$$(2.10) \quad J(z^k) - J(z^{k+1}) \geq \frac{w\varepsilon}{2}\|z^k - \tilde{x}^k\|^2 \quad \text{and} \quad J(z^k) > J(z^{k+1}) \quad (k \geq 0).$$

Since $\text{lev}_{J(z^0)} J$ is bounded and J is proper and lower semicontinuous, this verifies (i).

To verify (ii), we observe that summing (2.10) over $\ell = 0, \dots, k-1$ and telescoping gives

$$J(z^0) \geq J(z^k) + \frac{w\varepsilon}{2} \sum_{\ell=0}^{k-1} \|z^\ell - \tilde{x}^\ell\|^2 \geq \inf F + \frac{w\varepsilon}{2} \sum_{\ell=0}^{k-1} \|z^\ell - \tilde{x}^\ell\|^2 \quad (k \geq 1).$$

This implies $z^k - \tilde{x}^k \rightarrow 0$. We have assumed that $e^k \in \partial \tilde{J}_k(\tilde{x}^k)$ for some $e^k \rightarrow 0$. With $\partial \tilde{J}_k$ further expanded, using that

$$\nabla \left(\frac{1}{2}\|A_k(x)\|^2 \right) = \nabla A_k(x)A_k(x) = \nabla A(z^k)[A(z^k) + \nabla A(z^k)^*(x - z^k)],$$

this is to say

$$(2.11) \quad e^k \in \nabla A(z^k)[A(z^k) + \nabla A(z^k)^*(\tilde{x}^k - z^k)] + \partial F(\tilde{x}^k) + \beta(\tilde{x}^k - z^k).$$

Since $\{z^k\}_{k \in \mathbb{N}} \subset \text{lev}_{J(z^0)} J$, which by assumption is bounded, we can thus find a converging subsequence $z^{k_i} \rightarrow \hat{x}$ for some \hat{x} . Necessarily $\hat{x} \in \text{dom } F$.

Recall that the subdifferential mapping $x \mapsto \partial F(x)$ is outer semicontinuous [20], that is, if $q^{k_i} \in \partial F(z^{k_i})$ and also $q^{k_i} \rightarrow \hat{q}$, then $\hat{q} \in \partial F(\hat{x})$. As $A \in C^1(\text{dom } F; \mathbb{R}^M)$, passing to the subsequential limit in (2.11), using the outer semicontinuity and $e^k \rightarrow 0$, we obtain

$$(2.12) \quad 0 \in \nabla A(\hat{x})A(\hat{x}) + \partial F(\hat{x}).$$

Of course, $\nabla A(\hat{x})^*A(\hat{x}) = \nabla \left(\frac{1}{2}\|A(\hat{x})\|^2\right)$. By standard calculus rules for the Clarke subdifferential [11], (2.12) is therefore to say $0 \in \partial_C J(\hat{x})$. This proves (ii).

Finally, to prove (iii), let \hat{x}_1 and \hat{x}_2 be two different accumulation points of $\{z^k\}_{k \in \mathbb{N}}$. To reach a contradiction, suppose they would lie in two disjoint subsets U_1 and U_2 of V_L . Without loss of generality, we may assume that $V_L = U_1 \cup U_2$. Since V_L is closed (by J being lower semicontinuous and $\partial_C J$ outer semicontinuous), so are U_1 and U_2 . We can therefore find $\epsilon > 0$ such that $U_1^{2\epsilon}$ and $U_2^{2\epsilon}$ remain disjoint, where $U_j^\epsilon := U_j + B(0, \epsilon)$, ($j = 1, 2$). Let $L' := \inf_{x \in V \setminus (U_1^\epsilon \cup U_2^\epsilon)} J(x)$. Then $L' > L$. By definition of \hat{x}_1 and \hat{x}_2 as accumulation points, there exist subsequences $U_1^\epsilon \ni z^{k_i^1} \rightarrow \hat{x}_1$ and $U_2^\epsilon \ni z^{k_i^2} \rightarrow \hat{x}_2$ that satisfy $J(z^{k_i^1}) \rightarrow J(\hat{x}_1) = L < L'$ and $J(z^{k_i^2}) \rightarrow J(\hat{x}_2) = L < L'$. By passing to a subsequence, we may assume without loss of generality that $k_i^1 < k_i^2 < k_{i+1}^1$. Since $U_1^{2\epsilon}$ and $U_2^{2\epsilon}$ are disjoint, and $\|z^{k_i^1} - z^{k_i^2}\| = w\|z^{k_i^1} - \tilde{x}^{k_i^1}\| \rightarrow 0$ this implies for i large enough the existence of $k_i^* \in \mathbb{N}$ such that $z^{k_i^*} \in V \setminus (U_1^\epsilon \cup U_2^\epsilon)$ with $k_i^1 < k_i^* < k_i^2$. Then $J(z^{k_i^*}) \geq L' > L$. However, since $\{J(z^k)\}_{k \in \mathbb{N}}$ is decreasing and $J(z^{k_i^1}) \rightarrow L$, we also have $\limsup_{i \rightarrow \infty} J(z^{k_i^*}) \leq L$. This contradiction establishes that \hat{x}_1 and \hat{x}_2 must lie in the same disjoint component of V_L . \square

Remark 2.2 (More general data terms). Let $g : \mathbb{R}^n \rightarrow \mathbb{R}$ be subadditive and L -Lipschitz, for example, $g = \|\cdot\|_p$, $p \in [1, \infty]$. How could we replace $\frac{1}{2}\|A(x)\|^2$ by $g(A(x))$ in (1.1)? The inequality (2.9) is the crucial part of the proof to work with such an alternative fitting function. Due to subadditivity we have $g(A_k(z^{k+1})) - g(A(z^{k+1})) \geq -g(A(z^{k+1}) - A_k(z^{k+1}))$. If for some $C' > 0$ we assume

$$(2.13) \quad g(A(z^{k+1}) - A_k(z^{k+1})) \leq C'\|h\|^2,$$

then instead of (2.9) we obtain $g(A_k(z^{k+1})) - g(A(z^{k+1})) \geq -C'\|h\|^2$. The proof now goes through if we replace the third bound on w in (2.1) by $\frac{\beta - \epsilon}{2C'}$. For $g = \|\cdot\|_1$ and $C' = C$, (2.13) is simply [Assumption 2.1](#), so no additional assumptions are needed for that choice.

Remark 2.3 (Unique accumulation point under second-order growth conditions). If one of the accumulation points \hat{x} of $\{z^k\}_{k \in \mathbb{N}}$ is actually a unique local minimiser, for example, J satisfies a second-order growth condition around \hat{x} , then $S = \{\hat{x}\}$ forms a disjoint component of V_L . Consequently, \hat{x} has to be the unique accumulation point of $\{z^k\}_{k \in \mathbb{N}}$. It follows that the whole sequence converges to \hat{x} .

Remark 2.4 (Convergence with a larger relaxation parameter). *There are two obvious strategies to replace the relaxed variable z^{k+1} by $\tilde{z}^{k+1} := (1 - w_k)z^k + w_k\tilde{x}^k$ for some stepwise relaxation parameter w_k that violates the bounds (2.3):*

- a) *Since CA_{\max} in the third bound of (2.3) arises from (2.9), we can replace it by the exact “fractional linearisation error”*

$$\max \left\{ 0, \frac{\|A(\tilde{z}^{k+1})\|^2 - \|A_k(\tilde{z}^{k+1})\|^2}{2\|\tilde{z}^{k+1} - z^k\|^2} \right\} = \max \left\{ 0, \frac{\|A(\tilde{z}^{k+1})\|^2 - \|A_k(\tilde{z}^{k+1})\|^2}{2w_k\|z^k - \tilde{x}^k\|^2} \right\}.$$

This depends on w_k through \tilde{z}^{k+1} . We therefore need to perform a line search to find (the largest) w_k satisfying this condition subject to the first two bounds of (2.9).

- b) *If the inequality (2.10) holds for \tilde{z}^{k+1} in place of z^{k+1} . We can again use a line search to find a parameter $w_k \geq w$ satisfying this.*

3 SOLUTION OF THE INNER PROBLEM AND OTHER IMPLEMENTATION DETAILS

In this section, we discuss how to solve the subproblems (2.1) generated by Algorithm 2.1. Furthermore, we present a framework of how to apply RIPGN to (nonsmooth and nonconvex) regularized nonlinear least squares problems.

3.1 BALANCED PRIMAL DUAL PROXIMAL SPLITTING FOR THE LINEARISED SUBPROBLEM

To solve the nonsmooth but convex problems (2.2), we utilize a variant of the primal-dual proximal splitting (PDPS) due to Chambolle and Pock [9]). The basic version of the method applies to $\min G + F_1 \circ K_1$ for some convex G and F_1 and a linear operator K_1 . The function G and the Fenchel conjugate F_1^* need to have easily calculable proximal maps

$$\text{prox}_{tG}(z) := \arg \min_x G(x) + \frac{1}{2t}\|x - z\|,$$

where $t > 0$ is a step length parameter. However, our problem (2.2) with J_k defined in (2.1) will typically involve several operators; in case of total variation regularization of x ,

$$\min_x \frac{1}{2}\|A_k(x)\|^2 + \alpha\|\nabla_h x\| + \frac{\beta}{2}\|x - z^k\|.$$

Proximal maps for functions composed with operators are generally not easily calculable. Therefore, the linear part of A_k and the discretised gradient ∇_h will both have to go into K_1 ; it will consist of two different blocks with different scales, which moreover vary between the subproblems due to changing linearisations of A_k . We will therefore adapt the algorithm to the scales of these blocks following [46, 35].

3.2 SPATIALLY-ADAPTED PRIMAL-DUAL PROXIMAL SPLITTING

For convex, proper, lower semicontinuous $G : X \rightarrow \overline{\mathbb{R}}$, $F_1 : Y_1 \rightarrow \overline{\mathbb{R}}$, $F_2 : Y_2 \rightarrow \overline{\mathbb{R}}$ and linear operators $K_1 \in \mathbb{L}(X; Y_1)$, $K_2 \in \mathbb{L}(X; Y_2)$, on (finite-dimensional) Hilbert spaces X , Y_1 , and Y_2 , we consider

$$(3.1) \quad \min_{x \in X} G(x) + F_1(K_1x) + F_2(K_2x).$$

With $Kx := (K_1x, K_2x)$ and $y = (y_1, y_2) \in Y := Y_1 \times Y_2$, we can write the problem using the convex conjugates of F_1 and F_2 as

$$\min_{x \in X} \max_{y \in Y} G(x) + \langle Kx, y \rangle - F_1^*(y_1) - F_2^*(y_2).$$

Due to potentially different scales of the “blocks” y_1 and y_2 of y , we use two different dual step length parameters for numerical efficiency. This has been called “diagonal preconditioning” in [35] and “spatial adaptation” in [46]. The latter also introduces ways to perform acceleration when strong convexity is present in only some blocks. In either case, without acceleration, such a block-adapted method requires specifying step lengths $t, s_1, s_2 > 0$ satisfying

$$\text{Id} > t\Sigma^{1/2}KK^*\Sigma^{1/2} \quad \text{for} \quad \Sigma := \text{diag}(s_1 \text{Id}, s_2 \text{Id}),$$

where we write $\text{Id} : x \mapsto x$ for the identity operator. Since $KK^* = \begin{pmatrix} K_1K_1^* & K_1K_2^* \\ K_2K_1^* & K_2K_2^* \end{pmatrix}$, by Young’s inequality, this condition holds if for some $\lambda > 0$ and estimates $L_1 \geq \|K_1\|$ and $L_2 \geq \|K_2\|$,

$$(3.2) \quad 1 > (1 + \lambda)ts_1L_1^2 \quad \text{and} \quad 1 > (1 + \lambda^{-1})ts_2L_2^2.$$

Algorithm 3.1 specializes the spatially adapted or diagonally preconditioned PDPS to the two-block case and these step length conditions; for more general descriptions, stochastic sampling, and acceleration, we refer to [46]. A simple choice to satisfy (3.2) is to take for $\lambda = 1$, some $t > 0$, and small $\delta \in (0, 1)$,

$$(3.3) \quad s_1 = (1 - \delta)/[2tL_1^2] \quad \text{and} \quad s_2 = (1 - \delta)/[2tL_2^2].$$

Notice how larger $\|K_j\|$ will cause correspondingly smaller step length parameter s_j . This way the method can balance between differing scales of the different blocks of the dual variable.

The method has $O(1/N)$ convergence rate for an ergodic gap [46]. Since F_2^* is strongly convex, it would also be possible to update the parameters $t, s_1, s_2 > 0$ on each iteration to accelerate the method to a mixed $O(1/N^2) + O(1/N)$ convergence rate for y_2 [46].

3.3 RELAXED INEXACT PROXIMAL GAUSS-NEWTON

We now explain how we will use **Algorithm 3.1** to solve the sub-problems (2.2) for the RIPGN. We now assume that F has the structure $F(x) = F_2(K_2x) = F(x) + \delta_V(x)$, F_2 is convex, proper and lower semicontinuous, K_2 is linear, and δ_V is the $\{1, \infty\}$ -valued indicator function of a set $V \subset \mathbb{R}^N$. We will typically use V to model positivity constraints. We now formulate (2.2), namely

$$\min_x \frac{1}{2} \|A_k(x)\|^2 + F(x) + \frac{\beta}{2} \|x - z^k\|^2$$

Algorithm 3.1 Primal-dual proximal splitting with distinct step lengths for two dual blocks

Require: Convex, proper, lower semicontinuous $G : X \rightarrow \overline{\mathbb{R}}$, $F_1 : Y_1 \rightarrow \overline{\mathbb{R}}$, $F_2 : Y_2 \rightarrow \overline{\mathbb{R}}$ and linear operators $K_1 \in \mathbb{L}(X; Y_1)$, $K_2 \in \mathbb{L}(X; Y_2)$.

- 1: Choose step length parameters $t, s_1, s_2 > 0$ satisfying (3.2) for some upper bounds $L_1 \geq \|K_1\|$ and $L_2 \geq \|K_2\|$ and $\lambda > 0$.
 - 2: Choose initial iterates $x^0 \in X$, $y_1^0 \in Y_1$, $y_2^0 \in Y_2$.
 - 3: **for all** $i \geq 0$ **until** a stopping criterion is satisfied **do**
 - 4: $x^{i+1} := \text{prox}_{tG}(x^i - tK_1^*y_1^i - tK_2^*y_2^i)$
 - 5: $\bar{x}^{i+1} := 2x^{i+1} - x^i$
 - 6: $y_1^{i+1} := \text{prox}_{s_1F_1^*}(y_1^i + s_1K_1\bar{x}^{i+1})$
 - 7: $y_2^{i+1} := \text{prox}_{s_2F_2^*}(y_2^i + s_2K_2\bar{x}^{i+1})$
 - 8: **end for**
-

Algorithm 3.2 Relaxed inexact proximal Gauss–Newton for problem (1.1).

Require: Convex, proper, lower semicontinuous $F_2 : \mathbb{R}^n \rightarrow \overline{\mathbb{R}}$, linear and bounded $K_2 : \mathbb{R}^N \rightarrow \mathbb{R}^n$, convex $V \subset \mathbb{R}^N$, and $A \in C^1(V; \mathbb{R}^M)$.

Require: $w > 0$, $\delta \in (0, 1)$, $t > 0$, and $\beta > 0$.

- 1: Choose initial iterate z^0 .
 - 2: $s_2 := (1 - \delta)/[2t\|K_2\|^2]$
 - 3: **for all** $k \geq 0$ **until** a stopping criterion is satisfied **do**
 - 4: $K_1^k := \nabla A(z^k)^*$
 - 5: $b^k = \nabla A(z^k)^*z^k - A(z^k)$
 - 6: $s_1 := (1 - \delta)/[2t\|K_1^k\|^2]$
 - 7: Using Algorithm 3.1 with parameters t, s_1, s_2 and initial iterates $x^0 := z^k$, $y_1^0 := 0$, and $y_2^0 := 0$, find an approximate solution $\tilde{x}^k = x^i$ (for large i) to (3.4)
 - 8: $z^{k+1} := z^k + w(\tilde{x}^k - z^k)$
 - 9: **end for**
-

in the form (3.1) by taking $F_1^k(y) = \frac{1}{2}\|y - b^k\|^2$, $K_1^k = \nabla A(z^k)^*$, and $b^k = \nabla A(z^k)^*z^k - A(z^k)$. Furthermore, we place the proximal and the indicator term into $G^k(x) = \delta_V(x) + \frac{\beta}{2}\|x - z^k\|^2$. We added superscript k to F_1 , K_1 , and G to highlight that these terms depend on the outer iteration. Now the linearised problem (2.2) can be written

$$(3.4) \quad \arg \min_x G^k(x) + F_1^k(K_1^k x) + F_2(K_2 x).$$

This has the form (3.1) and can be solved with Algorithm 3.1 using step parameters (3.3).

Note that in Theorem 2.1 we may consider δ_V as a part of F . However, from computational stand-point, it is usually more efficient to include it into G .

The whole process of solving (1.1), the relaxed inexact proximal Gauss–Newton method, is described in Algorithm 3.2. Here we would like to stress that $A(z)$ and $F(z)$ depend on the application. In the next section, we discuss specific choices of these functions in the case of electrical impedance tomography.

4 APPLICATION TO ELECTRICAL IMPEDANCE TOMOGRAPHY

We give a brief review of the EIT forward model and its finite element (FE) approximation in a case where measurements consist of electric currents corresponding to a set of potential excitations. We treat the inverse conductivity problem of EIT as a regularized nonlinear least squares problem for which we describe three different regularization schemes. In this section, as a deviation of the previous section, the unknown of interest is written σ instead of z or x to be consistent with typical notation for electrical conductivity.

4.1 FORWARD MODEL OF EIT

Due to our measurement equipment, we derive the forward model of EIT in such way that it solves the current through each electrode, given the conductivity within the domain and potential at each electrode. More specifically, in each excitation, one of the electrodes on object's surface is set to a known electric potential, and the rest of the electrodes are connected to ground. Corresponding to each excitation, electric currents through all grounded electrodes are measured.

As the result of the FE approximation, we obtain a nonlinear operator $I(\sigma)$, which together measurement vector I^m and an additional weight matrix L_A , forms the data fidelity term $A(\sigma)$ (see below). For details of the FE approximation, we refer to [49].

Given the electrical conductivity σ within domain Ω and a potential U_k^p at each electrode e_k during excitation p , the forward problem of EIT is to solve the current I_k^p through each electrode. This requires solving also the spatially distributed electric potential u^p inside the domain. The most accurate physically realizable way to model this is the Complete Electrode Model (CEM) [10]. For existence and uniqueness of CEM see [41]. With $\chi = (\chi_1, \chi_2, \chi_3)$ the spatial coordinates within the domain $\Omega \subset \mathbb{R}^3$, CEM is described by a set of equations

$$(4.1a) \quad \nabla \cdot (\sigma(\chi) \nabla u^p(\chi)) = 0 (\chi \in \Omega), \quad u^p(\chi) + \zeta_k \sigma \frac{\partial u^p(\chi)}{\partial \hat{n}} = U_k^p \quad (\chi \in \partial\Omega_{e_k}),$$

$$(4.1b) \quad \int_{\partial\Omega_{e_k}} \sigma \frac{\partial u^p(\chi)}{\partial \hat{n}} dS = -I_k^p, \quad \text{and} \quad \sigma \frac{\partial u^p(\chi)}{\partial \hat{n}} = 0, \quad \left(\chi \in \partial\Omega \setminus \bigcup_{k=1}^L \partial\Omega_{e_k} \right).$$

where $\partial\Omega_{e_k}$ is the part of the $\partial\Omega$ covered by k 'th electrode, ζ_k is contact impedance, \hat{n} is the outward unit normal of Ω , and L is the number of electrodes. In addition, the currents I_k^p are required to satisfy Kirchhoff's law $\sum_{k=1}^L I_k^p = 0$. From here on, we assume the contact impedances to be known, $\zeta_k = 10^{-7} \Omega$, as the actual contact impedances in the measurement setups used in this study are negligible.

In order to approximate the solution of the boundary value problem (4.1) numerically, we utilize Galerkin finite element method (FEM). Following the scheme described in thesis [49], we write a variational form of the system (4.1). Moreover, we use a finite dimensional approximation of the electric potential u as $u^p(\chi) = \sum_{j=1}^{N_u} u_j^p \phi_j(\chi)$ and write the vector of electrode currents for excitation p as $I^p = \sum_{j=1}^{L-1} \tilde{I}_j^p n_j$ to ensure that the Kirchhoff's current law is fulfilled. Here ϕ_j is a basis function for presenting the electric potential, and n_j , $j = 1, \dots, L-1$, are vectors that form a basis for the electrode currents. As in a typical Galerkin scheme, ϕ_j and n_j are also

used as test functions in the variational form. The FE approximation, i.e., the coefficient vector $\theta^p = (u_1^p, \dots, u_N^p, \tilde{I}_1^p, \dots, \tilde{I}_{L-1}^p)$, is obtained as a solution of the linear system

$$(4.2) \quad D\theta^p = \tilde{U}^p, \quad \text{where} \quad D = \begin{pmatrix} D_1 & 0 \\ D_2 & D_3 \end{pmatrix} \in \mathbb{R}^{(N+L-1) \times (N+L-1)},$$

and the elements of the blocks D_1 , D_2 and D_3 are

$$\begin{aligned} [D_1]_{ij} &= \int_{\Omega} \sigma(\chi) \nabla \phi_j(\chi) \cdot \nabla \phi_i(\chi) \, dV + \sum_{k=1}^L \frac{1}{\zeta_k} \int_{e_k} \phi_j(\chi) \phi_i(\chi) \, dS, \\ [D_2]_{kj} &= - \sum_{k=1}^L \frac{1}{\zeta_k} \int_{e_k} \phi_j(\chi) (n_k)_k \, dS = - \left(\frac{1}{\zeta_1} \int_{e_1} \phi_j(\chi) \, dS - \frac{1}{\zeta_{k+1}} \int_{e_{k+1}} \phi_j(\chi) \, dS \right) \\ [D_3]_{kl} &= \sum_{k=1}^L (n_l)_k (n_k)_k = \begin{cases} 1, & k \neq l \\ 2, & k = l \end{cases} \end{aligned}$$

where $i, j = 1, \dots, N$; $j = 1, \dots, N$; and $k, l = 1, \dots, L-1$. The vector \tilde{U}^p is computed from the known electrode potentials as

$$(4.3) \quad [\tilde{U}^p]_i = \begin{cases} \sum_{k=1}^L \frac{U_k^p}{\zeta_k} \int_{e_k} \phi_i(\chi) \, dS, & i = 1, \dots, N \\ \frac{U_{i+1}^p}{\zeta_{i+1}} |e_{i+1}| - \frac{U_1^p}{\zeta_1} |e_1|, & i = N+1, \dots, N+L-1. \end{cases}$$

Note that the electrode currents I^p are obtained from (4.2) by first solving the coefficient vector $\theta^p = D(\sigma)^{-1} \tilde{U}^p$ then multiplying $I^p = \mathcal{K} \theta^p$ where $\mathcal{K} \in \mathbb{R}^{L \times (N+L-1)}$, $\mathcal{K} = [0, \dots, 0, n_1, \dots, n_{L-1}]$. Now the operator A can be written as

$$A(\sigma) = L_A (I(\sigma) - I^m),$$

where L_A arises from the factorization of the inverse noise covariance matrix (precision matrix) $W = L_A^* L_A$ [14], $I(\sigma) = (I(\sigma)^1, \dots, I(\sigma)^L) \in \mathbb{R}^{L^2}$ is a vector containing currents from all excitations, and I^m is the measurement vector corresponding to I . For the linearisation, specifically the components used in (3.4), we have $K_1^k = L_A \nabla I(\sigma^k)^*$ and $b^k = L_A (I^m + \nabla_{\sigma} I(\sigma^k)^* \sigma^k - I(\sigma^k))$.

Finally, we also discretise the conductivity, setting $\sigma = \sum_{i=1}^N \sigma_i \varphi_i$, where φ_i are linear basis functions. Note that \tilde{U}^p is constant with respect to the factors σ_i , thus the partial derivatives $\frac{\partial I^p}{\partial \sigma_i}$ can be solved from

$$0 = \frac{\partial \tilde{U}^p}{\partial \sigma_i} = \frac{\partial D \theta^p}{\partial \sigma_i} = \frac{\partial D}{\partial \sigma_i} \theta^p + D \frac{\partial \theta^p}{\partial \sigma_i} \iff \frac{\partial I^p}{\partial \sigma_i} = \frac{\partial \mathcal{K} \theta^p}{\partial \sigma_i} = -\mathcal{K} D^{-1} \frac{\partial D}{\partial \sigma_i} \theta^p.$$

For further details on the computation of the Jacobian see [Appendix E](#).

4.2 REGULARIZATION AND CONSTRAINTS

Next we introduce three different regularization schemes for EIT. We utilize these schemes in [Section 5](#). The first scheme comprises of smoothness-promoting L^2 -regularization and a

barrier function to approximate the positivity constraint. We use this scheme to compare the RIPGN against Newton's method. The other two schemes comprise of total variation (TV) with a positivity constraint, and smoothed TV with the barrier function. The latter is used to compare RIPGN against Newton's method in TV-regularized setting, and the smooth models against nonsmooth models. For a detailed description on how to compute the required proximal mappings for Algorithm 3.1 see <http://proximity-operator.net> and [5]. Additional mappings are listed in Appendix D.

4.2.1 SMOOTHNESS-PROMOTING REGULARIZATION WITH A BARRIER

We take the first regulariser

$$F_\Gamma(\vec{\sigma}) := \|R_\Gamma(\vec{\sigma} - \vec{\sigma}_m)\|^2,$$

where $\vec{\sigma}_m$ is the expected value of $\vec{\sigma}$, and $\vec{\sigma} = (\sigma_1, \dots, \sigma_N)$ is the vector of FE factors of σ . The matrix R_Γ is defined by inverse factorization $(R_\Gamma^* R_\Gamma)^{-1} = \Gamma$ of a Gaussian kernel $\Gamma_{i,j} = ae^{-\frac{\|x_i - x_j\|^2}{2b}}$ [29]. Furthermore, we introduce a piecewise polynomial barrier function

$$B_{\min}(\sigma) := \frac{1}{2} \|L_{\min}(\sigma)(\vec{\sigma} - \sigma_{\min})\|^2, \quad \text{with} \quad [L_{\min}]_{ij}(\sigma) := \begin{cases} l_{\min}, & \text{where } i=j \text{ and } \sigma_i < \sigma_{\min} \\ 0, & \text{otherwise,} \end{cases}$$

where l_{\min} is a coefficient that determines the strength of the barrier function. Now the convex component in (1.1) is $F(\sigma) = F_\Gamma(R_\Gamma \sigma) + B_{\min}(\sigma)$. As B_{\min} is diagonal, in the subproblems, it is computationally more efficient to include it into G^k . Thus, for formulating the two-block PDPS for the subproblems as in Section 3.3, we take $F_2(y) = F_\Gamma(y)$, $K_2 \sigma = R_\Gamma \vec{\sigma}$, and $G^k(\sigma) = B_{\min}(\sigma) + \delta_V(\sigma) + \frac{\beta}{2} \|\sigma - \sigma^k\|^2$.

4.2.2 TV REGULARIZATION AND NONSMOOTH CONSTRAINTS

In the second scheme we apply nonsmooth total variation regularization with positivity constraints. Since σ is continuous by its finite element construction, its isotropic total variation (TV) [38] can be written as

$$\text{TV}(\sigma) = \int_{\Omega} |\nabla \sigma(\chi)| dV,$$

where $|x| = \sqrt{x_1^2 + x_2^2 + x_3^2}$ is the Euclidean spatial norm. In linear basis, the spatial gradient of σ is constant within an element, meaning $\frac{\partial \sigma(\chi)}{\partial \chi_1} = \left(\frac{\partial \sigma}{\partial \chi_1}\right)_i$ if χ belongs to element i , and the integration yields

$$\text{TV}(\sigma) = \sum_{i=1}^{N_E} V_i \sqrt{\left(\frac{\partial \sigma}{\partial \chi_1}\right)_i^2 + \left(\frac{\partial \sigma}{\partial \chi_2}\right)_i^2 + \left(\frac{\partial \sigma}{\partial \chi_3}\right)_i^2},$$

where V_i is the volume of the i 'th element and N_E is the number of elements in FE basis. This can be expressed

$$\text{TV}(\sigma) = \sum_{i=1}^{N_E} \sqrt{(R_1 \vec{\sigma})_i^2 + (R_2 \vec{\sigma})_i^2 + (R_3 \vec{\sigma})_i^2} =: \|R_\nabla \sigma\|_{2,1},$$

where $R_\nabla \sigma := [(R_1 \vec{\sigma})^T \ (R_2 \vec{\sigma})^T \ (R_3 \vec{\sigma})^T]^T$ and the components (i, j) of $R_l \in \mathbb{R}^{N_E \times N}$ for $l = 1, 2, 3$ are computed from the basis functions φ_j as

$$[R_l]_{ij} = \begin{cases} V_i \frac{\partial \varphi_j}{\partial \chi^l}, & \varphi_j \text{ when is non-zero in element } i, \\ 0, & \text{otherwise.} \end{cases}$$

For formulating the two-block PDPS for the subproblems as in [Section 3.3](#), we now take $F_2(y) = \alpha \|y\|_{2,1}$, $K_2 = R_\nabla$, and $G^k(\sigma) = \delta_V(\sigma) + \frac{\beta}{2} \|\sigma - \sigma^k\|^2$.

In some examples of [Section 5](#), we use TV regularization on two-dimensional domains. In those cases, the volume V_i of the element i is replaced by the element surface area and the spatial difference operators, R_1 and R_2 , are computed from the two-dimensional basis functions. Operator R_3 is dropped.

4.2.3 SMOOTHED TV REGULARIZATION AND BARRIER FUNCTION

As the last regularization scheme, we introduce a smoothed version of TV and semismooth barrier functions. The smoothed TV can be written as

$$\tilde{TV}(\sigma) = \|f(\sigma)\|_1 \quad \text{with} \quad [f(\sigma)]_i = \sqrt{(R_1 \vec{\sigma})_i^2 + (R_2 \vec{\sigma})_i^2 + (R_3 \vec{\sigma})_i^2 + \gamma}.$$

Here, γ is a smoothing parameter that we set to $\gamma = 10^{-7}$. We also introduce a maximum barrier $B_{\max}(\sigma)$, by an obvious modification of the minimum barrier $B_{\min}(\sigma)$ described above. Now the component F in (1.1) is $F(\sigma) = \alpha \tilde{TV}(\sigma) + B_{\min}(\sigma) + B_{\max}(\sigma)$, and for the subproblems we have $F_2(y) = \alpha \|y\|_1$, $K_2(\sigma) = f(\sigma)$, and $G^k(\sigma) = B_{\min}(\sigma) + B_{\max}(\sigma) + \delta_V(\sigma) + \frac{\beta}{2} \|\sigma - \sigma^k\|^2$. Note that with these notations, the operator K in the subproblem (2.2) is nonlinear. Hence we solve it using a variant [Algorithm 3.1](#) for nonlinear K from [44, 30].

5 NUMERICAL AND EXPERIMENTAL STUDIES

We evaluate the proposed relaxed inexact proximal Gauss–Newton (RIPGN) method numerically in EIT image reconstruction. In the first set of numerical studies, Cases 1–3 ([Section 5.2](#)), we compare RIPGN against Newton’s method and NL-PDPS in a circular 2D geometry and in Case 6 ([Section 5.4](#)), we demonstrate viability of RIPGN to three-dimensional EIT reconstruction. In Cases 4–5, [Section 5.3](#), we evaluate the performance of RIPGN with experimental data obtained through EIT-based sensing skin technique. The sensing skin is a surface sensor developed for structural health monitoring: In this technique, the structure is coated with conductive paint and the conductivity of the paint-layer is reconstructed using EIT. If the structure’s surface breaks, for example, by cracking, it damages also the paint-layer, and this damage is detected by EIT [18]. We include further experiments in [Appendices B](#) and [C](#).

5.1 COMPUTATIONAL ASPECTS

In the numerical studies, we evaluate the convergence of RIPGN ([Algorithm 3.2](#)) with multiple relaxation parameters w and use static values for the parameters δ , t , and β . We set δ to an

Table 1: Parameters used in each test case. σ^{ref} is the value of the homogeneous estimate computed from reference measurements.

Case(s)	Setup	Data	Regularisation	$L_A(i, i)$	α	l_{\min}	l_{\max}	σ_{\min}	σ_{\max}	V_{\min}	V_{\max}
1	2D Water tank	Synthetic	Smooth	$5 \cdot 10^4$	-	$10^2 \sqrt{2J(\sigma^1)}$	-	10^{-4}	-	10^{-8}	10^{12}
2	2D Water tank	Synthetic	Smoothed TV	$5 \cdot 10^4$	10	$10^2 \sqrt{2J(\sigma^1)}$	$10^2 \sqrt{2J(\sigma^1)}$	10^{-4}	10^{10}	10^{-8}	10^{12}
3	2D Water tank	Synthetic	TV	$5 \cdot 10^4$	10	-	-	-	-	10^{-4}	10^{12}
4	Sensing skin	Measured	Smoothed TV	100	1/4	$5\sqrt{2J(\sigma^1)}$	$10^{-1} \sqrt{2J(\sigma^1)}$	10^{-4}	σ^{ref}	10^{-8}	10^{12}
5	Sensing skin	Measured	TV	100	1/4	-	-	-	-	10^{-4}	σ^{ref}
6	3D Water tank	Synthetic	TV	$5 \cdot 10^4$	10	-	-	-	-	10^{-4}	10^{12}

arbitrary small value $\delta = 0.01$ to satisfy (3.2), choose $t = 10^{-6}$ by evaluating the convergence of the first subproblem of Case 3 with multiple step parameters (see Section 5.2.5), and set β to a small value $\beta = 10^{-10}$; in our experience, β has similar impact on the convergence of the Algorithm 3.2 as the relaxation parameter w . Every linearised subproblem is solved to 6000 iterations.

We start the RIPGN, Newton, and NL-PDPS iterations from a homogeneous estimate σ^1 . Furthermore, we introduce minimum and maximum constraints, V_{\min} and V_{\max} , by defining the domain V as a hypercube $V = \{\sigma \in \mathbb{R}^N : V_{\min} \leq \sigma_i \leq V_{\max}, i = 1, 2, \dots, N\}$. Table 1 shows the parameters that vary between the cases. Note that in this section, we denote the first index as $k = 1$ instead of $k = 0$.

In synthetic tests, Cases 1–3 and 6, we compute the relative error of the estimated conductivity $\hat{\sigma}$ with respect to the true conductivity σ_{true} as $\text{RE} = \|\hat{\sigma} - \sigma_{\text{true}}\| / \|\sigma_{\text{true}}\| \cdot 100\%$. Note, however, that due to the simulated measurement noise and the modeling errors caused by the differing mesh sparsities, the true conductivity is often quite far from the actual minimum of the objective function. To highlight this, we compute the objective function at the true conductivity by evaluating the true conductivity at the nodes of the mesh we use in the forward solution. We also compute the relative error of this interpolation, to assess how well the original conductivity could be presented in the forward solution mesh.

We perform all computations in MATLAB 2017b with dual Intel Xeon E5649 @ 2.53/2.93 GHz CPUs and with 99 GB RAM (1333 Mhz ECC DDR3). We implement crucial components of the construction of the matrix D and the Jacobian ∇A in C++. We compute the forward solution (4.2), the equation $\hat{K}D^{-1}$ for the Jacobian and the linear system for Newton’s method through LU decomposition using UMFPACK [13]. In Case 6, we compute the forward solution using BiCGSTAB.

To catch the stagnation of the RIPGN and Newton’s method, we initially stop the iteration if an iterate z^k decreases the value of the objective function less than 0.5, i.e., if $J(\sigma^k) - J(\sigma^{k-1}) < 0.5$. However, in order to ensure that the iteration does not end prematurely, we compute additional two iterates to check if one of those decreases the objective function by at least 0.5. If they do, we continue the iteration normally, and if not, we discard these two iterates and take the initial stopping iterate as the estimated solution. We employ this stagnation check after eighth iteration to ensure that at least 10 iterations are computed. For NL-PDPS, we extend these conditions to 700 and 300, respectively. We note that, as in many previous EIT studies [48], line search is used in Newton’s method, as the method did not converge within reasonable time with a constant step parameter.

5.2 NUMERICAL 2D EIT STUDIES

In Cases 1–3, the geometry of the domain Ω resembles shallow water tank. The diameter of the tank is 24 cm and the height is 7 cm. Furthermore, the tank has sixteen evenly placed electrodes on the surface; the width and height of the electrodes are 2.5 cm and 7 cm, respectively.

The conductivity inside the tank is constant along the vertical axis, and hence, although the EIT forward model is three-dimensional, the conductivity is two-dimensionally distributed. In the forward model, we map the 2D conductivity to 3D by linear interpolation.

When simulating the measurement data, we present the electrical conductivity in a piecewise linear basis using a tetrahedral mesh consisting 84052 nodes and we approximate the electric potential in a second order polynomial basis consisting 629513 nodes. In the reconstruction, we approximate the 2D conductivity in a piecewise linear basis with triangular 2D mesh of 1117 nodes; for the forward solver, we map this 2D distribution to piecewise linear 3D distribution (tetrahedral mesh consisting 8189 nodes). Furthermore, we approximate the electric potential with second order polynomial basis functions in a mesh with 56986 nodes.

To simulate actual measurements more realistically, we add Gaussian distributed noise, with std of $0.005 |I_i|$, to each simulated measurement I_i .

5.2.1 CASE 1: SMOOTHNESS-PROMOTING REGULARIZATION & NEWTON'S METHOD

We first evaluate the RIPGN against Newton's method on a smooth optimization problem. We use the smoothness promoting regularization (Scheme 1; Section 4.2.1). Furthermore, to match the regularization, the true conductivity is also smooth (Figure 2, left): We generate the true conductivity by drawing a sample from a multivariate Gaussian distribution expressing spatial smoothness. This distribution is of the form described in Section 4.2.1, and its expectation as well as the parameters of the covariance matrix are chosen to be same as in the model used in regularization. We note, however, that since the FE mesh used in inversion is sparser than that in the data simulation, the true conductivity is a not a realization from a model that corresponds to the regularizing function.

Figure 1 shows the value of the objective function as a function of iteration number k and computational time t for RIPGN method corresponding to five relaxation parameters w and for the Newton's method. Table 2 lists the number of iterations required for convergence, value of the objective function at the last iterate, computational time and relative error corresponding to each of these estimates. Figure 2 illustrates the reconstructed images.

Figure 1 and Table 2 show that in Case 1, Newton's method and RIPGN with $w \leq 3/4$ converge. The reconstructions have small relative errors, as shown by Table 2. Smaller relaxation parameters result in increased number of iterations, which in turn increases the computational times, as expected. RIPGN with $w = 3/4$ converges in around 7 minutes, while Newton's method converges in about same amount of iterations, but the computation of each iterate is considerably longer, taking around 37 minutes to converge. Hence, although subproblems are solved exactly in Newton's method, we need the same amount of iterations for convergence as with RIPGN, which solves subproblems inexactly. Longer computational times with Newton's method are mostly due to the line search method.

Figure 2 shows that the reconstruction from converging iterations are visually very close to

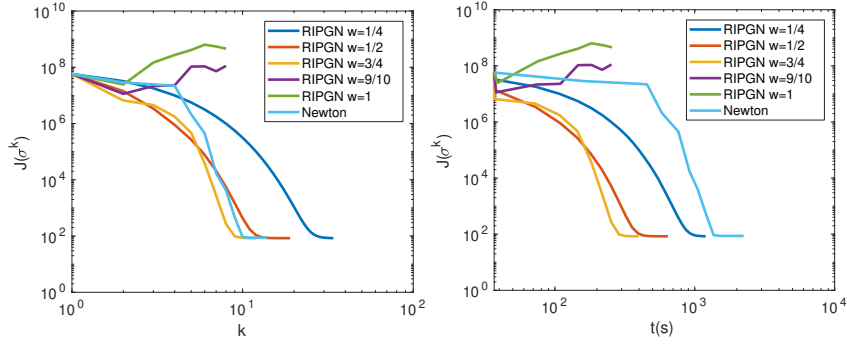


Figure 1: Case 1. Value of the objective function J as function of iteration number k (left), and computational time t (right) for the RIPGN and Newton's method.

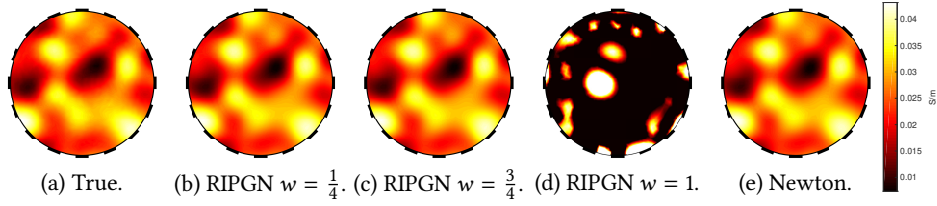


Figure 2: Case 1. True conductivity (a), RIPGN-based reconstructions with relaxation parameters $w = 1/4$ (b), $w = 3/4$ (c), $w = 1$ (d), and the Newton-based reconstruction (e).

Table 2: Case 1. The number of iterations required for convergence, value of the objective function at the last iterate, computational time, and relative error of the estimate for the RIPGN and Newton's method.

Algorithm	Iterations (K)	$J(\hat{\sigma})$	Time (s)	RE(%)
RIPGN $w = 1/4$	34	84.069	1197.4	2.1864
RIPGN $w = 1/2$	19	84.059	642.58	2.1895
RIPGN $w = 3/4$	12	84.512	398.23	2.1975
RIPGN $w = 9/10$	8	$1.1179 \cdot 10^8$	254.1	73.431
RIPGN $w = 1$	8	$4.5842 \cdot 10^8$	255.97	103.68
Newton	14	86.7	2236.2	2.1969

the true conductivity. With step parameters $w = 9/10$ and $w = 1$, the RIPGN reconstructions diverge. Convergence, indeed, cannot be expected for relaxation parameters $w \approx 1$ due to the bound (2.3) in Theorem 2.1.

As mentioned in Section 5.1, we also evaluate the objective function at the true conductivity. This gives $J(\sigma_{\text{true}}) = 1.2057 \cdot 10^5$ and a 0.9294% relative error, meaning that although the true conductivity can be presented quite accurately in the forward solution mesh, the best presentation is very likely far off from the actual minimum of the objective function.

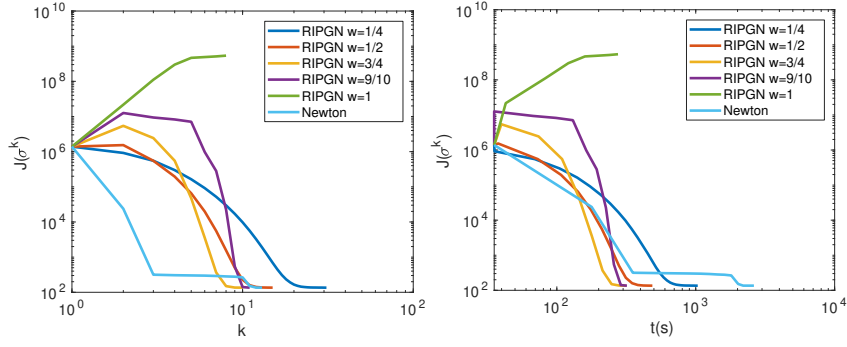


Figure 3: Case 2. Value of the objective function J as function of iteration number k (left), and computational time t (right) for the RIPGN and Newton's method.

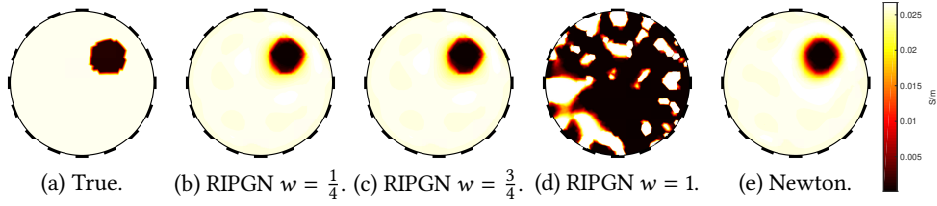


Figure 4: Case 2. True conductivity (a), RIPGN-based reconstructions with relaxation parameters $w = 1/4$ (b), $w = 3/4$ (c), $w = 1$ (d), and the Newton-based reconstruction (e).

5.2.2 CASE 2: SMOOTHED TV REGULARIZATION \mathcal{C}^2 COMPARISON WITH NEWTON'S METHOD

Because standard Newton's method cannot be used on non-smooth problems (such as those induced by regularization Scheme 2, Section 4.2.2), in Case 2, we compare RIPGN to Newton's method in Scheme 3 (Section 4.2.3); a smoothed version of Scheme 2. In Case 2, the true target contains a circular inclusion of low conductivity (10^{-3} S/m) on a constant background with conductivity of 0.028 S/m.

Figure 3 and Table 3 show that in Case 2, Newton's method takes around 44 minutes to converge while RIPGN with relaxation parameter $w = 3/4$ and $w = 9/10$ takes around 5–6 minutes. RIPGN diverges again with relaxation parameter $w = 1$. The relative errors in Case 2 are larger than in Case 1. This is expected, as the conductivity in Case 1 was a draw from a distribution with statistical properties that corresponded to the regularization that was used. These errors are further increased as the smooth shapes in Case 1 tend to be more accurately representable with linear interpolation than sharp-edged inclusion in Case 2. The reconstructed images (Figure 4) are, however, fairly accurate. Evaluating the objective function at the true conductivity gives $J(\sigma_{\text{true}}) = 8.6491 \cdot 10^4$ with 4.6023% relative error.

Table 3: Case 2. The number of iterations required for convergence, value of the objective function at the last iterate, computational time, and relative error of the estimate for the RIPGN and Newton's method.

Algorithm	Iterations (K)	$J(\hat{\sigma})$	Time (s)	RE(%)
RIPGN $w = 1/4$	31	135.35	1033.7	6.5056
RIPGN $w = 1/2$	15	135.61	487.21	6.5088
RIPGN $w = 3/4$	10	135.51	315.76	6.5164
RIPGN $w = 9/10$	10	135.63	319.6	6.5162
RIPGN $w = 1$	8	$5.386 \cdot 10^8$	275.66	151.06
Newton	13	135.77	2622.4	7.1371

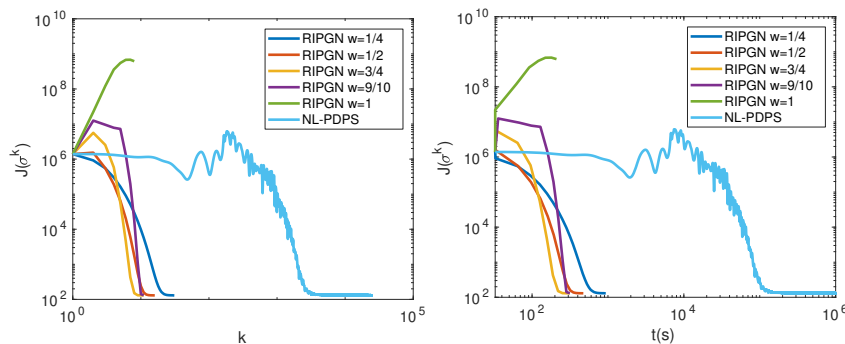


Figure 5: Case 3. Value of the objective function J as function of iteration number k (left), and computational time t (right) for the RIPGN and NL-PDPS.

5.2.3 CASE 3: TV REGULARIZATION & COMPARISON WITH NL-PDPS

In Case 3, we compare RIPGN with NL-PDPS [44]. We use the nonsmooth regularization (Scheme 2; Section 4.2.2). The target conductivity in Case 3 is the same as in Case 2.

Figure 6 shows no visual differences between the reconstruction computed with RIPGN ($w < 1$) and the reconstruction computed with NL-PDPS. However, Figure 5 and Table 4 show that NL-PDPS takes over a week and a half to solve the problem with the desired accuracy, while RIPGN (with $w = 3/4$ or $w = 9/10$) takes less than 6 minutes. It should be noted though that the total amount of iterations, including the 6000 in each RIPGN linearisation, is considerably fewer with NL-PDPS. This is consistent with earlier studies [44, 12].

Finally, Figure 6 and Table 4 show that the unsmoothed total variation slightly improves the reconstruction quality and the relative error from Case 2 (cf. Figure 4 and Table 3).

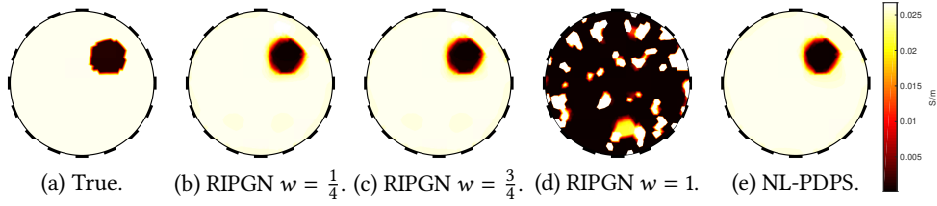


Figure 6: Case 3. True conductivity (a), RIPGN-based reconstructions with relaxation parameters $w = 1/4$ (b), $w = 3/4$ (c), $w = 1$ (d), and the NL-PDPS-based reconstruction (e).

Table 4: Case 3. The number of iterations required for convergence, value of the objective function at the last iterate, computational time, and relative error of the estimate for the RIPGN and the NL-PDPS.

Algorithm	Iterations (K)	$J(\hat{\sigma})$	Time (s)	RE(%)
RIPGN $w = 1/4$	31	129.48	935.31	5.8401
RIPGN $w = 1/2$	16	129.97	473.62	5.8436
RIPGN $w = 3/4$	11	129.9	313.4	5.8466
RIPGN $w = 9/10$	11	130.24	314.73	5.8533
RIPGN $w = 1$	8	$7.1417 \cdot 10^8$	225.87	334.68
NL-PDPS	24221	130.56	$9.9253 \cdot 10^5$	5.9157

5.2.4 EFFECTS OF THE SMOOTHED TV

Next we compare the solutions of the smoothed TV scheme to those of the (nonsmooth) TV scheme. Although the differences between the reconstructions in Figure 4 and Figure 6 appear small, closer inspection reveals these to be fundamental. Figure 7 shows the true conductivity and three profiles of the true conductivity that are taken along the dashed line. The Figure 7 also shows profiles from the solutions computed using Newton's method, RIPGN with smoothed TV and RIPGN with TV.

The profiles in Figure 7 illustrate that the solution corresponding to smoothed TV is spatially smoother than that corresponding to non-smoothed TV—the former fails to track the sharp edges in the conductivity. We remind that all solutions are actually piecewise linear due to the choice of basis functions.

5.2.5 SUBPROBLEM PARAMETER SELECTION AND BALANCING

In Cases 1–3, we used step parameter $t = 10^{-6}$ in the linear solver. We chose this step parameter by evaluating the rate of convergence of the first subproblem in Case 3 with multiple step parameters t , and then selecting the one that converges fastest. Figure 8 (left) shows the value of the objective function at the approximative solution $J_1(\tilde{x}^1)$ after 6000 iterations. Furthermore, to illustrate the differences between the balanced and the non-balanced method, the figure shows the value of $J_1(\tilde{x}^1)$ when the problem is solved without balancing, i.e., with $s_1 = s_2 = (tL^2)^{-1}$.

On the right in Figure 8, solid lines indicate the value of $J_k(\tilde{x}^k)$ when the problem is solved

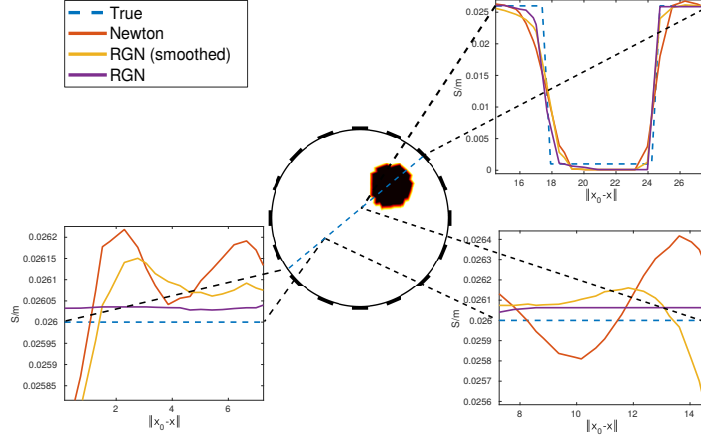


Figure 7: The differences between the smoothed and unsmoothed total variation are distinguishable on closer inspection. Conductivity profile is highlighted with a dashed blue line. Same profile is also taken from smooth Newton and RIPGN reconstructions and nonsmooth RIPGN reconstruction.

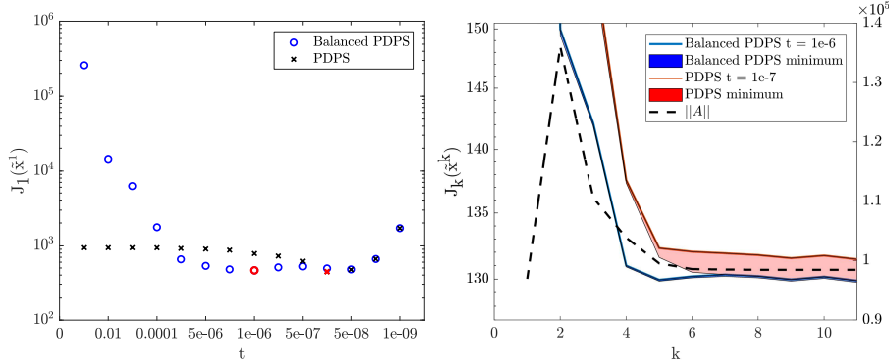


Figure 8: Left: Value of the objective function in the first linearised problem at the minimum point estimate \hat{x} as a function of step parameter t . The step parameters $t = 10^{-6}$ and $t = 10^{-7}$ are highlighted in red. Right: Value of the objective function of linearised problem k at the \hat{x}^k with $t = 10^{-6}$ for the balanced algorithm and $t = 10^{-7}$ non-balanced. Area around the curves highlight the minimum value with any t . The dashed line represents the operator norm of ∇A .

using both the balanced and the non-balanced methods with step parameters $t = 10^{-6}$ and $t = 10^{-7}$ respectively. Areas below the curves show the minimum with any of the tested parameters. For this experiment, the outer iteration is advanced with relaxation parameter $w = 3/4$ using solutions from the balanced method with $t = 10^{-6}$. For the curiosity, the operator norm of ∇A is also shown in the figure.

Figure 8 shows that although both methods converge almost equally in the first subproblem, the balanced method outperforms normal PDPS in the subsequent problems. Furthermore,

Figure 8 shows that unlike with the non-balanced PDPS, in the balanced PDPS, the optimal step parameter remains almost unchanged at every linearisation.

5.3 EXPERIMENTAL STUDIES

The measurement device we use in the experimental studies is manufactured by Rocsole Ltd. (www.rocsole.com). This device utilizes a typical ECT measurement principle in which each electrode is sequentially set to a known sinusoidal potential, while the others remain grounded. The currents induced by the potential differences are then sampled, in this case with 1 MHz sampling frequency, and the amplitude of the induced current is computed from the samples using discrete Fourier transform. Here the excitation frequency is set to 39 kHz and measurements used in the reconstruction are time averages of the computed amplitudes over one minute time period.

5.3.1 CASES 4-5: SENSING SKIN & CRACK DETECTION

In Case 4, we test RIPGN in a crack detection problem arising from EIT-based sensing skins (see [18]). Computationally this crack detection problem differs from the inclusion detection in a typical water tank geometry, because cracks cause sharp but spatially narrow inclusions of low conductivity on the background conductivity of the paint layer. Furthermore, the conductive paint is far from being homogeneous in thickness and consequently, the background conductivity is inhomogeneous. To take into account this inhomogeneity we follow an approximative data correction approach proposed in [18]. In addition, we exploit the fact that the cracks never increase the conductivity, allowing us to constrain the conductivity from above.

The sensing skin used in the study is painted with Kontakt Chemie EMI 35 conductive graphite paint onto a rectangular plexiglass. The side lengths of the plexiglass are 44 cm and 42 cm and each side has seven 2.5 cm \times 1.25 cm electrodes. Furthermore, four 2.5 cm \times 2.5 cm electrodes are placed in the middle of the sensing skin.

From the sensing skin measurements, we compute a smoothed TV solution with Newton's method and RIPGN (Case 4), and a nonsmooth TV solutions with RIPGN (Case 5). The triangular mesh used in the computations has 3147 nodes for the conductivity represented in a piecewise linear basis and 12281 nodes for the electric potential in second order basis. Parameters used in these cases are shown in Table 1.

Figure 10 (left) shows a photograph of the sensing skin in Case 4. The crack in the photograph is highlighted in red as the crack is very narrow.

Figure 9 shows that for every relaxation parameter RIPGN converges considerably better than with $w = 1$ in Cases 1-3. However, the value of the objective function oscillates slightly over the last few iterations when $w > 1/2$. The better convergence with relaxation parameter $w \leq 1/2$ is also confirmed by Table 5. The objective function with Newton's method converges to similar values as RIPGN with the larger step parameters. Note that in this case, the iteration time with Newton's method is considerably shorter than in Cases 1-3 due to the two-dimensional forward model. Furthermore, Figure 10 shows that the reconstructed images capture the shape and length of the crack rather well. In this example, the effect of relaxation parameter to the quality of RIPGN-based reconstruction is very small, and even the difference between the RIPGN-

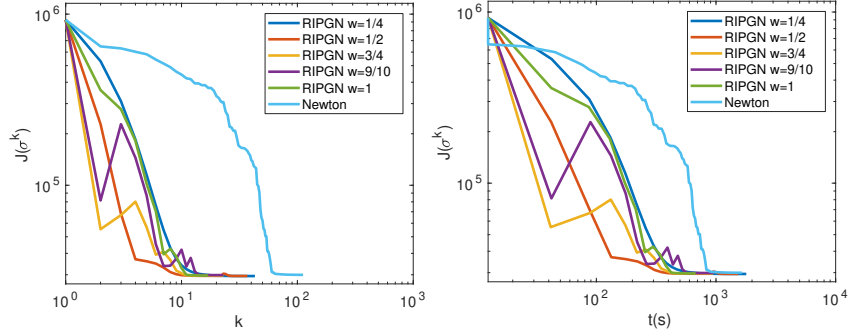


Figure 9: Case 4. Value of the objective function J as function of iteration number k (left), and computational time t (right) for the RIPGN and Newton's method.

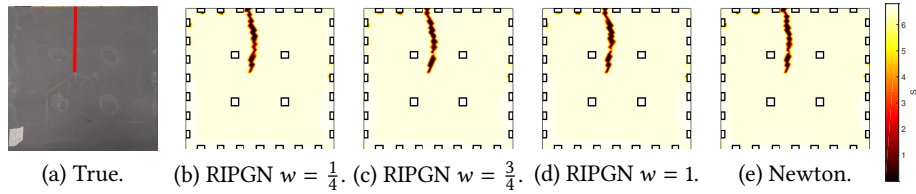


Figure 10: Case 4. Photo of the sensing skin (crack highlighted) (a), RIPGN-based reconstructions with relaxation parameters $w = 1/4$ (b), $w = 3/4$ (c), $w = 1$ (d), and the Newton-based reconstruction (e).

Table 5: Case 4. The number of iterations required for convergence, value of the objective function at the last iterate, and computational time for the RIPGN and the Newton's method.

Algorithm	Iterations (K)	$J(\hat{\sigma})$	Time (s)
RIPGN $w = 1/4$	43	29478	1791.2
RIPGN $w = 1/2$	37	29504	1538.9
RIPGN $w = 3/4$	23	29681	950.08
RIPGN $w = 9/10$	23	29858	954.99
RIPGN $w = 1$	17	29679	676.2
Newton	112	29949	1642.3

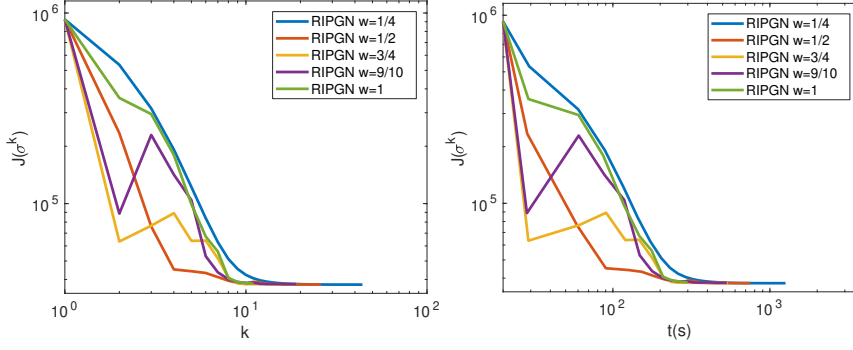


Figure 11: Case 5. Value of the objective function J as function of iteration number k (left), and computational time t (right) for the RIPGN.

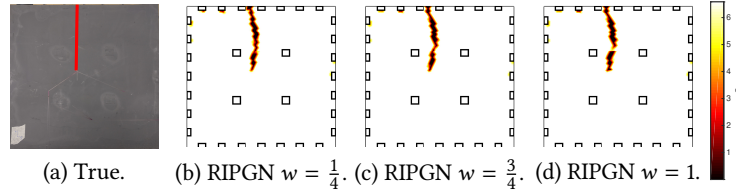


Figure 12: Case 5. Photo of the sensing skin (crack highlighted) (a), RIPGN-based reconstructions with relaxation parameters $w = 1/4$ (b), $w = 3/4$ (c), $w = 1$ (d).

Table 6: Case 5. The number of iterations required for convergence, value of the objective function at the last iterate, and computational time for the RIPGN and the Newton's method.

Algorithm	Iterations (K)	$J(\hat{\sigma})$	Time (s)
RIPGN $w = 1/4$	44	37601	1256.8
RIPGN $w = 1/2$	26	37629	750.21
RIPGN $w = 3/4$	19	37801	540.46
RIPGN $w = 9/10$	19	37812	531.91
RIPGN $w = 1$	11	38015	299.03

and Newton-based reconstructions is somewhat negligible. We note, again, that the choices of the optimization method and relaxation parameter do have an effect on the converge and computation speed, as shown by Table 5.

In Case 5, the sensing skin dataset used in Cases 4 is used to reconstruct TV regularized solution (Scheme 2) with RIPGN. The results are shown in Figures 11–12 and Table 6. Comparing these results with results in Case 4 shows that the contrast between the crack and the background conductivities is higher when the non-smooth model is used (Scheme 2). Again, the computational times are shorter than in the smoothed case (see Section 5.2.3). Apart from these differences, the results are fairly similar to smoothed TV.

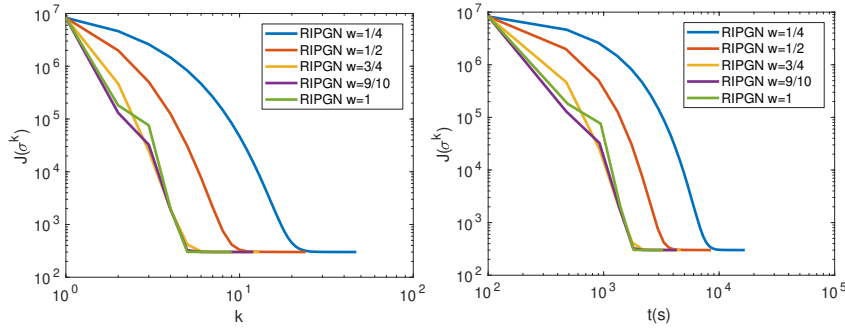


Figure 13: Case 6. Value of the objective function J as function of iteration number k (left), and computational time t (right) for the RIPGN.

5.4 NUMERICAL 3D EIT STUDY

In Case 6, we evaluate the feasibility of RIPGN to three-dimensional EIT. The geometry resembles a cylinder that has a radius of 14 cm and a height of 26 cm. Furthermore, the cylinder has four horizontal layers of electrodes on the surface. Each layer contains 10 evenly placed square electrodes with side length of 3 cm. The gap between each electrode layer is 4 cm. The cylinder contains a resistive inclusion with conductivity of 10^{-3} S/m on a background conductivity of 0.028 S/m.

In the data simulation we present the electrical conductivity in a piecewise linear basis with 210860 nodes, and the electric potential in a second order polynomial basis with 1632276 nodes. Furthermore, the inversion mesh has 18835 nodes for the conductivity and 135504 nodes for the potential. The reconstructions are computed with Scheme 3 (Section 4.2.2).

Figure 14 shows that in Case 6 the relaxation parameter has negligible impact on the reconstruction quality and the reconstructions look very similar to the true conductivity distribution. Figure 13 and Table 7 show that, even in terms of the final value of the objective function, RIPGN converges similarly with every step parameter. Clearly, in this case we get no benefits for lowering the step parameter as lowering it only increases the amount of iterations required to satisfy the convergence criteria; with step parameter $w = 1/4$ it takes 47 iterations, while with $w = 1$ it takes only 9. This is also reflected in the computational times. Furthermore, these computational times are considerably longer compared to the previous cases as number of nodes, elements, and electrodes in the model are greater. As in the previous synthetic cases, the true conductivity is known and evaluating the objective function at σ_{true} yields $J(\sigma_{\text{true}}) = 7.0220 \cdot 10^4$. Furthermore, the relative error is $\text{RE} = 1.250\%$.

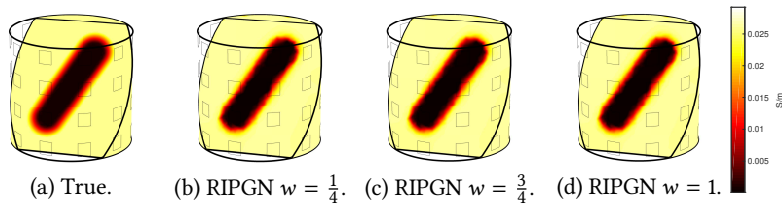


Figure 14: Case 6. True conductivity (a), RIPGN-based reconstructions with relaxation parameters $w = 1/4$ (b), $w = 3/4$ (c), and $w = 1$ (d). A tomographic slice of the distribution along plane $p(x) = -x_1 - x_2 + x_3 = 14$ is shown in the figures.

Table 7: Case 6. The number of iterations required for convergence, value of the objective function at the last iterate, computational time, and relative error of the estimate for the RIPGN and the NL-PDPS.

Algorithm	Iterations (K)	$J(\hat{\sigma})$	Time (s)	RE(%)
RIPGN $w = 1/4$	47	300.5643	$1.6681 \cdot 10^4$	2.8742
RIPGN $w = 1/2$	24	300.6393	$8.4881 \cdot 10^3$	2.8737
RIPGN $w = 3/4$	13	300.8226	$4.6491 \cdot 10^3$	2.8768
RIPGN $w = 9/10$	12	301.1563	$4.3054 \cdot 10^3$	2.8752
RIPGN $w = 1$	9	300.6904	$3.2748 \cdot 10^3$	2.8747

6 CONCLUSIONS

We proposed a novel relaxed inexact proximal Gauss–Newton (RIPGN) method, and studied it both theoretically and numerically. We applied the method to image reconstruction from electrical impedance tomography (EIT) measurements which is a large-scale non-linear inverse problem governed by a PDE model.

We showed that the RIPGN converges to a disjoint set of Clarke critical points under conditions that hold for typical inverse problems. Furthermore, we presented a framework for the application of RIPGN to such problems. We confirmed the efficacy of the RIPGN on synthetic and experimental EIT data. These studies showed that by adjusting the relaxation parameter w , the iterates generated by the RIPGN converge to solutions that meaningful for EIT applications. Furthermore, when w was appropriately selected, the RIPGN estimates were significantly faster to compute than more conventional estimates produced by Newton’s method in the smooth case and the NL-PDPS in the nonsmooth case.

Overall, RIPGN combined with (NL-)PDPS offers a flexible framework to solve various non-convex and nonsmooth problems. In EIT, the greatest advantage of the method was achieved with nonsmooth TV regularization. Following the implementation of this work, RIPGN method can be straightforwardly adopted also to a variety of other optimization problems—those associated with other non-smooth regularization schemes as well as other imaging/reconstruction applications yielding non-convex optimization problems. In the future, this may enable handling such large-scale problems without need for smoothing and/or reducing the model complexity, which both can lead to loss of contrast and appearance of imaging artefacts. Moreover, the

RIPGN might even enable—via computational speed-up—realizations of high-contrast real-time imaging in some applications.

ACKNOWLEDGMENTS

This project has received funding from the European Union’s Horizon 2020 research and innovation programme under grant agreement No 764810. The research was also funded by the Academy of Finland (Centre of Excellence of Inverse Modelling and Imaging, 2018-2025, project 303801).

T. Valkonen has been supported by Academy of Finland grants 314701 and 320022 as well as Escuela Politécnica Nacional internal grant PIJ-18-03.

APPENDIX A GEOMETRIC JUSTIFICATION FOR ZERO PROXIMAL PARAMETER

We now improve [Theorem 2.1](#) by showing that we can take the proximal parameter $\beta = 0$ provided e^k is small enough and a critical point satisfies certain geometric conditions. We will then also obtain local convergence to this specific critical point. The rough plan of work is to show that [\(2.4\)](#) holds under these conditions for some $\beta > 0$ despite the algorithm employing $\beta = 0$. Throughout, we take J as in [\(1.1\)](#) and for brevity write

$$G(x) := \frac{1}{2}\|A(x)\|^2 \quad \text{and} \quad G_k(x) := \frac{1}{2}\|A_k(x)\|^2 = \frac{1}{2}\|A(z^k) + \nabla A(z^k)(x - z^k)\|^2.$$

We will for some $\rho > 0$ on [line 3](#) of [Algorithm 2.1](#),

$$(A.1) \quad \text{solve (2.1) for } \tilde{x}^k \text{ to such accuracy that } \|e^k\| \leq \rho\|\tilde{x}^k - z^k\| \text{ for some } e^k \in \partial J_k(\tilde{x}^k).$$

Lemma A.1. *Suppose [Assumption 2.1](#) holds. In [Algorithm 2.1](#) use (A.1). If $q^k := e^k - \nabla G_k(\tilde{x}^k) \in \partial F(\tilde{x}^k)$ satisfies*

$$F(z^k) - F(\tilde{x}^k) \geq \langle q^k, z^k - \tilde{x}^k \rangle + \frac{1}{2}\|z^k - \tilde{x}^k\|_{\Gamma_k}^2$$

for some operator Γ_k such that $\nabla A(z^k)\nabla A(z^k)^* + \Gamma_k \geq (2\rho + \beta)I$ for some $\beta > 0$, then [\(2.4\)](#) holds. If [\(2.3\)](#) holds for this β , then the conclusions of [Theorem 2.1](#) hold.

Proof. We have $q^k = e^k - \nabla A_k(\tilde{x}^k)A_k(\tilde{x}^k) = e^k - \nabla A(z^k)[A(z^k) + \nabla A(z^k)^*(\tilde{x}^k - z^k)]$. Since we take $\beta = 0$ in the algorithm, $e^k \in \partial J_k(\tilde{x}^k)$. Therefore

$$\begin{aligned} J(z^k) - J_k(\tilde{x}^k) &= \frac{1}{2}\|A(z^k)\|^2 - \frac{1}{2}\|A_k(\tilde{x}^k)\|^2 + F(z^k) - F(\tilde{x}^k) \\ &\geq \frac{1}{2}\|A(z^k)\|^2 - \frac{1}{2}\|A_k(\tilde{x}^k)\|^2 + \langle q^k, z^k - \tilde{x}^k \rangle + \frac{1}{2}\|z^k - \tilde{x}^k\|_{\Gamma_k}^2 \\ &= \frac{1}{2}\|A(z^k)\|^2 - \frac{1}{2}\|A_k(\tilde{x}^k)\|^2 - \langle A_k(\tilde{x}^k), \nabla A_k(\tilde{x}^k)^*(z^k - \tilde{x}^k) \rangle \\ &\quad + \langle e^k, z^k - \tilde{x}^k \rangle + \frac{1}{2}\|z^k - \tilde{x}^k\|_{\Gamma_k}^2. \end{aligned}$$

We expand and simplify

$$\begin{aligned}
& \frac{1}{2} \|A(z^k)\|^2 - \frac{1}{2} \|A_k(\tilde{x}^k)\|^2 - \langle A_k(\tilde{x}^k), \nabla A_k(\tilde{x}^k)^*(z^k - \tilde{x}^k) \rangle \\
&= \frac{1}{2} \|A(z^k)\|^2 - \frac{1}{2} \|A(z^k) + \nabla A(z^k)^*(\tilde{x}^k - z^k)\|^2 \\
&\quad - \langle A(z^k) + \nabla A(z^k)^*(\tilde{x}^k - z^k), \nabla A(z^k)^*(z^k - \tilde{x}^k) \rangle \\
&= \frac{1}{2} \|\nabla A(z^k)^*(\tilde{x}^k - z^k)\|^2.
\end{aligned}$$

Using the assumption $\|e^k\| \leq \rho \|\tilde{x}^k - z^k\|$ thus

$$J(z^k) - J_k(\tilde{x}^k) \geq \frac{1}{2} \|z^k - \tilde{x}^k\|_{\nabla A(z^k) \nabla A(z^k)^* + \Gamma_k}^2 - \rho \|z^k - \tilde{x}^k\|^2.$$

This and the assumption $\nabla A(z^k) \nabla A(z^k)^* + \Gamma_k \geq (2\rho + \beta) \text{Id}$ prove (2.4). \square

We now merely assume the conditions of the lemma in the limit:

Theorem A.2. *Suppose $\hat{q} := -\nabla G(\hat{x}) \in \partial F(\hat{x})$ satisfies $F(z) - F(\hat{x}) \geq \langle \hat{q}, z - \hat{x} \rangle + \frac{1}{2} \|z - \hat{x}\|_\Gamma^2$ for all z and some operator Γ such that $\nabla A(\hat{x}) \nabla A(\hat{x})^* + \Gamma \geq (2\rho + \theta) \text{Id}$ for some $\theta, \rho > 0$. Take any $\beta \in (0, \theta)$ satisfying (2.3) and initialize z^0 close enough to \hat{x} . In Algorithm 2.1 use (A.1). Then the conclusions of Theorem 2.1 hold.*

Proof. Let $q^k := e^k - \nabla G_k(\tilde{x}^k) \in \partial F(\tilde{x}^k)$. By the outer semicontinuity of the convex subdifferential ∂F [20], and the continuity of ∇A and A , it is clear that for all $\epsilon > 0$ that there exists $r' > 0$ such that $\|\tilde{x}^k - \hat{x}\|, \|z^k - \hat{x}\| \leq r'$ ensures $\|q^k - \hat{q}\| \leq \epsilon$, $\nabla A(z^k) \nabla A(z^k)^* + \Gamma \geq (2\rho + \beta) \text{Id}$, and $F(z^k) - F(\tilde{x}^k) \geq \langle q^k, z^k - \tilde{x}^k \rangle + \frac{1}{2} \|z^k - \tilde{x}^k\|_\Gamma^2$. Therefore, if we can ensure that $\{z^k\}_{k \in \mathbb{N}}, \{\tilde{x}^k\}_{k \in \mathbb{N}} \subset B(\hat{x}, r')$ for some small enough $r' > 0$, the claim follows from Lemma A.1.

Since $\tilde{x}^k = w^{-1}(z^{k+1} - z^k) + z^k$, it suffices to show for some small $r > 0$, for all $k \in \mathbb{N}$, that $z^k \in B(\hat{x}, r)$, and that $\|z^k - z^{k-1}\| \leq r$. We moreover claim that $J(z^k) \leq J(\hat{x}) + \delta r^2 \epsilon / (2w)$ for some $\delta \in (0, 1]$. We prove all of this by induction. The induction basis follows from initializing $z^0 = z^{-1}$ close enough to \hat{x} , that is, with $r > 0$ small enough. For the induction step, assume the claim holds for k . We will prove that it holds for $k + 1$. Indeed, by Lemma A.1, (2.4) holds for k . Thus, by the proof Theorem 2.1, (2.10) holds for k : $J(z^k) - J(z^{k+1}) > \frac{w\epsilon}{2} \|z^k - \tilde{x}^k\|^2$. By the inductive assumption and $J(z^{k+1}) \geq J(\hat{x})$, thus

$$\frac{\epsilon}{2w} \|z^{k+1} - z^k\|^2 \leq J(z^k) - J(z^{k+1}) \leq J(z^k) - J(\hat{x}) \leq \frac{\delta r^2 \epsilon}{2w}.$$

This shows $\|z^{k+1} - z^k\| \leq r$. Since $J(z^{k+1}) \leq J(z^k)$, also $J(z^{k+1}) \leq J(\hat{x}) + \delta r^2 \epsilon / (2w)$.

It remains to prove $z^{k+1} \in B(\hat{x}, r)$. We have $\hat{q} = -\nabla A(\hat{x}) A(\hat{x})$ and for $z \in B(\hat{x}, r'')$ with r'' small enough, $A(\hat{x}) = A(z) + \nabla A(\hat{x})(\hat{x} - z) + O(\|z - \hat{x}\|^2)$. Therefore, arguing similarly to Lemma A.1,

$$J(z) - J(\hat{x}) \geq \frac{1}{2} \|z - \hat{x}\|_{\nabla A(\hat{x}) \nabla A(\hat{x})^* + \Gamma}^2 - O(\|z - \hat{x}\|^2) \geq c \|z - \hat{x}\|^2$$

for any $0 < c < \theta + 2\rho$ and $z \in B(\widehat{x}, r'')$. Since $z^k \in B(\widehat{x}, r)$ and, as we have shown, $\|z^{k+1} - z^k\| \leq r$, we have $z^{k+1} \in B(\widehat{x}, 2r)$. Therefore, taking $r < r''/2$, we have $z^{k+1} \in B(\widehat{x}, r'')$. Taking $z = z^{k+1}$, it now follows

$$\frac{\delta r^2 \varepsilon}{2\omega} \geq J(z^k) - J(\widehat{x}) \geq J(z^{k+1}) - J(\widehat{x}) \geq c \|z^{k+1} - \widehat{x}\|^2.$$

Therefore, if $\delta > 0$ is small enough, $z^{k+1} \in B(\widehat{x}, r)$. This finishes the induction and the proof. \square

We now need to obtain some local strong convexity of F . We concentrate on total variation; in the EIT problems that we consider in Section 4, more local strong convexity could be obtained from the box constraints. Related geometric approaches in [45, 25, 26, 28, 16] show the local linear convergence of convex optimization methods, and even globally to submanifolds. The next lemma establishes the fundamental idea of the approach. The condition in it has been related to the *strong (metric) subregularity* of the subdifferentials ∂F [1].

Lemma A.3. *Let $F : \mathbb{R}^n \rightarrow \overline{\mathbb{R}}$ be convex and $q \in \text{int } \partial F(x)$ for some $x \in \mathbb{R}^n$. Then for any $\gamma > 0$, for some $\rho > 0$, $F(z) - F(x) \geq \langle q, z - x \rangle + \frac{\gamma}{2} \|z - x\|^2$ for all $z \in B(x, \rho)$.*

Proof. By the definition of the convex subdifferential,

$$F(z) - F(x) \geq \sup_{q' \in \partial F(x)} \langle q', z - x \rangle = \langle q, z - x \rangle + \sup_{q' \in \partial F(x)} \langle q' - q, z - x \rangle$$

Because $q \in \text{int } \partial F(x)$, there exists $\varepsilon > 0$ such that $B(q, \varepsilon) \subset \partial F(x)$. We can therefore take $q' = q + \frac{\gamma}{2}(z - x)$ provided $\frac{\gamma}{2} \|z - x\| \leq \varepsilon$, that is, if $z \in B(x, \rho)$ for $\rho = 2\varepsilon/\gamma$. This immediately yields the claim. \square

For the next lemma, we recall we that $\|g\|_{p,1} := \sum_{i=1}^n \|g_i\|_p$, where $g \in \mathbb{R}^{n \times m}$ and we write $g_i \cdot = (g_{1i}, \dots, g_{mi})$.

Lemma A.4. *Let $F(x) := \|Wx\|_{p,1}$ for some $W \in \mathbb{R}^{(n \times m) \times n}$. Assume for all $i = 1, \dots, n$ the existence of $k_i \in \{1, \dots, n\}$ such that $[Wx]_{k_i \cdot} = 0$ and $W_{k_i \cdot, i} \neq 0$. Then $\text{int } \partial F(x) \neq \emptyset$.*

Proof. We have $\partial F(x) = W^* \partial \|\cdot\|_{p,1}(Wx)$, where $\partial \|\cdot\|_{p,1}(g) = \prod_{i=1}^n \partial \|\cdot\|_p(g_i \cdot)$. From our assumptions, for all $i = 1, \dots, n$ we have $\partial \|\cdot\|_p([Wx]_{k_i \cdot}) = B_{p^*}$ for the dual unit ball $B_{p^*} := \{q \in \mathbb{R}^m \mid \|q\|_{p^*} \leq 1\}$ with $1/p + 1/p^* = 1$. Hence, for all $i = 1, \dots, n$, the projection of $\partial F(x)$ to the i :th coordinate,

$$\begin{aligned} [\partial F(x)]_i &= [W^* \partial \|\cdot\|_{p,1}(Wx)]_i = \sum_{k=1}^n \langle W_{k \cdot, i}, [\partial \|\cdot\|_{p,1}(Wx)]_{k \cdot} \rangle \\ &= \sum_{k \neq k_i} \langle W_{k \cdot, i}, [\partial \|\cdot\|_{p,1}(Wx)]_{k \cdot} \rangle + \langle W_{k_i \cdot, i}, B_{p^*} \rangle. \end{aligned}$$

The last term has non-empty interior. Hence $\text{int}[\partial F(x)]_i \neq \emptyset$ for all $i = 1, \dots, n$. Since $\text{int } \partial F(x) \supset \prod_{k=1}^n \text{int}[\partial F(x)]_k$, the claim follows. \square

The next theorem shows that forward-differences discretised total variation is locally strongly convex around a “strictly piecewise constant” \widehat{x} .

Theorem A.5. Let $F(x) = \|\nabla_h x\|_{p,1}$ for $\nabla_h \in \mathbb{R}^{(n_1 \times n_2 \times 2) \times (n_1 \times n_2)}$ the forward differences operator with (discrete) Neumann boundary conditions and cell width $h > 0$. Assume that $\hat{x} \in n_1 \times n_2$ is strictly piecewise constant in the sense that for each pixel coordinate $(i, j) \in \{1, \dots, n_1\} \times \{1, \dots, n_2\}$ there exists a neighboring pixel coordinate

$$(k_{ij}, k_{ij}) \in \mathcal{N}_{i,j} := \{1, \dots, n_1\} \times \{1, \dots, n_2\} \cap \{(i, j), (i+1, j), (i, j+1), (i-1, j), (i, j-1)\}$$

with $[\nabla_h \hat{x}]_{k_{ij}k_{ij}} = 0$. Then $\text{int } \partial F(\hat{x}) \neq \emptyset$. In particular, for any $\gamma > 0$ and $\hat{q} \in \text{int } \partial F(\hat{x})$ and $\rho > 0$ such that $F(z) - F(\hat{x}) \geq \langle \hat{q}, z - \hat{x} \rangle + \frac{\gamma}{2} \|z - \hat{x}\|^2$ for all $z \in B(\hat{x}, \rho)$.

Proof. The strict piecewise constancy assumption verifies with $W = \nabla_h$ for all $i = 1, \dots, n_1$ and $j = 1, \dots, n_2$ the existence of $(k, k) = (k_{ij}, k_{ij}) \in \{1, \dots, n_1\} \times \{1, \dots, n_2\}$ such that $[W\hat{x}]_{kk} = 0$ and $W_{kk, \cdot, ij} \neq 0$. The non-empty interior of the subdifferential is now a consequence of Lemma A.4. The strong convexity at \hat{x} then follows from Lemma A.3. \square

If the solution is not strictly piecewise constant at some pixel, then the fitting term G has to provide the corresponding second-order growth. This is reasonable to expect, as total variation whenever allowed by the fitting term, would produce piecewise constant solutions.

Corollary A.6. Let $F(x) = \|\nabla_h x\|_{p,1}$ for $\nabla_h \in \mathbb{R}^{(n_1 \times n_2 \times 2) \times (n_1 \times n_2)}$ the forward differences operator with (discrete) Neumann boundary conditions. Let $\hat{x} \in [\partial_C J]^{-1}(0)$ be a Clarke-critical point of J . For all pixels $(i, j) \in \{1, \dots, n_1\} \times \{1, \dots, n_2\}$ such that $-\nabla G(\hat{x})_{ij} \notin \text{int}[\partial F(\hat{x})]_{ij}$ (in particular, if (i, j) fails the strict piecewise constancy assumption of Theorem A.5 in the sense that there exists no $(k_{ij}, k_{ij}) \in \mathcal{N}_{i,j}$ with $[\nabla_h \hat{x}]_{k_{ij}k_{ij}} = 0$), assume that $[\nabla A(\hat{x}) \nabla A(\hat{x})^*]_{ij,ij} \geq 2\rho + \theta$ for some $\theta > 0$. Take any $\beta \in (0, \theta)$ satisfying (2.3) and initialize z^0 close enough to \hat{x} . In Algorithm 2.1 use (A.1). Then the conclusions of Theorem 2.1 hold.

Proof. With $\hat{q} := -\nabla G(\hat{x})$ let \mathcal{S} be the set of pixel coordinates (i, j) satisfy $\hat{q}_{ij} \in \text{int}[\partial F(\hat{x})]_{ij}$. Then, if $(i, j) \notin \mathcal{S}$, we have $-\nabla G(\hat{x})_{ij} \in \text{bd}[\partial F(\hat{x})]_{ij}$. We take $\gamma = 2\rho + \theta$ and Γ such that $[\Gamma]_{ij,ij} = \gamma$ for pixels $(i, j) \in \mathcal{S}$ and zero in all other entries. Then, proceeding as in Lemma A.3, we deduce the existence of $\rho > 0$ such that

$$F(z) - F(\hat{x}) \geq \langle \hat{q}, z - \hat{x} \rangle + \frac{1}{2} \|z - \hat{x}\|_{\Gamma}^2 \quad (z \in B(\hat{x}, \rho)).$$

By our assumptions we also have $[\nabla A(\hat{x}) \nabla A(\hat{x})^*]_{ij,ij} \geq \Gamma = \gamma \text{Id} = (2\rho + \theta) \text{Id}$. The rest follows from Theorem A.2. \square

APPENDIX B ADDITIONAL CASES (7–12)

Case 7 is complementary to Case 2; it uses the same geometry and same regularization scheme (Scheme 3) but true conductivity is different. In this case, the target contains a square-shaped inclusion with conductivity of 10^{-3} S/m and a conductive circular inclusion with conductivity 0.28 S/m. The conductivity of the constant background is 0.028 S/m. The results of Case 3 are shown in Figures 15–16, and Table 8.

Figure 15 shows that RIPGN with relaxation parameters $w = 1$ and $w = 9/10$ does not converge. Furthermore, the relative error is considerably higher as the total variation regularization tends

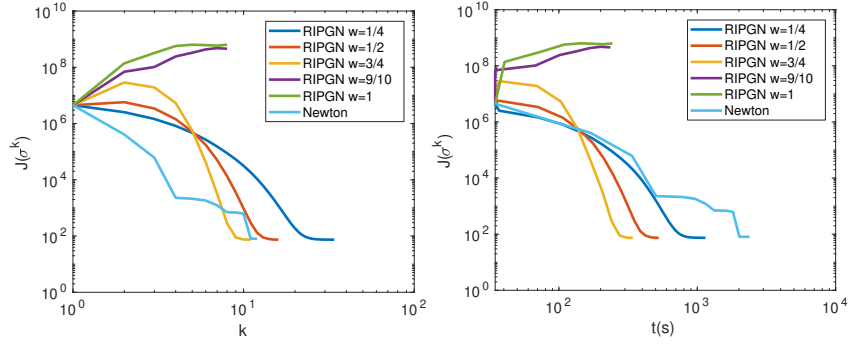


Figure 15: Case 7. Value of the objective function J as function of iteration number k (left), and computational time t (right) for the RIPGN and Newton's method.

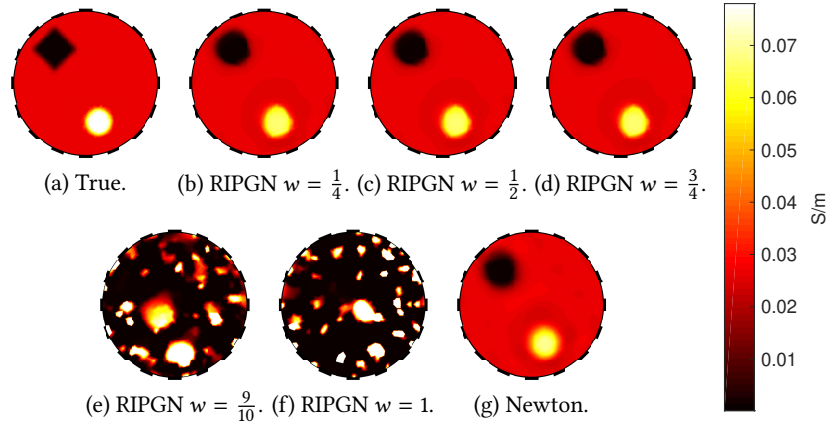


Figure 16: Case 7. True conductivity (a), RIPGN-based reconstructions corresponding to five relaxation parameters w (b)–(f), and the Newton-based reconstruction (g).

to round the shape of the resistive inclusion [17]. In addition, the range of the conductivity is flattened. It is also notable that the fit in this case is better in terms of the objective function than in Case 2. Interpolating the true conductivity into the inversion mesh gives $J(\sigma_{\text{true}}) = 1.0918 \cdot 10^5$ and $\text{RE} = 3.8874 \%$.

Similarly to Case 7, Case 8 is complementary to Case 3. In this case, the comparison to NL-PDPS is omitted due to excessively long computational times of NL-PDPS. The results of Case 8 are shown in Figure 17–18, and Table 9. Again, the computational times and the relative errors are improved when compared to the smoothed TV solutions in Case 3 (cf. Table 8), similarly to what happened between Cases 2 and 4. Also, the differences in computational times and relative errors between Case 4 and 5 are analogous to differences between Case 2 and 3.

Table 8: Case 7. The number of iterations required for convergence, value of the objective function at the last iterate, computational time, and relative error of the estimate for the RIPGN and Newton's method.

Algorithm	Iterations (K)	$J(\hat{\sigma})$	Time (s)	RE(%)
RIPGN $w = 1/4$	34	73.942	1145.2	10.012
RIPGN $w = 1/2$	16	74.238	526.82	10.035
RIPGN $w = 3/4$	11	74.02	342.07	10.069
RIPGN $w = 9/10$	8	$4.5458 \cdot 10^8$	235.21	166.67
RIPGN $w = 1$	8	$6.3257 \cdot 10^8$	243.83	295.45
Newton	12	80.658	2387.1	11.161

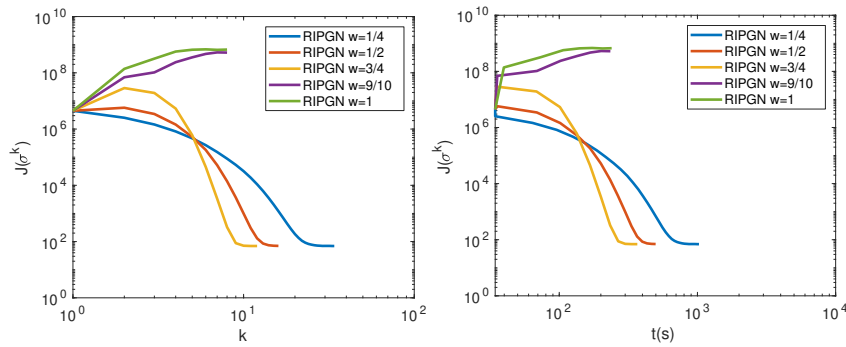


Figure 17: Case 8. Value of the objective function J as function of iteration number k (left), and computational time t (right) for the RIPGN.

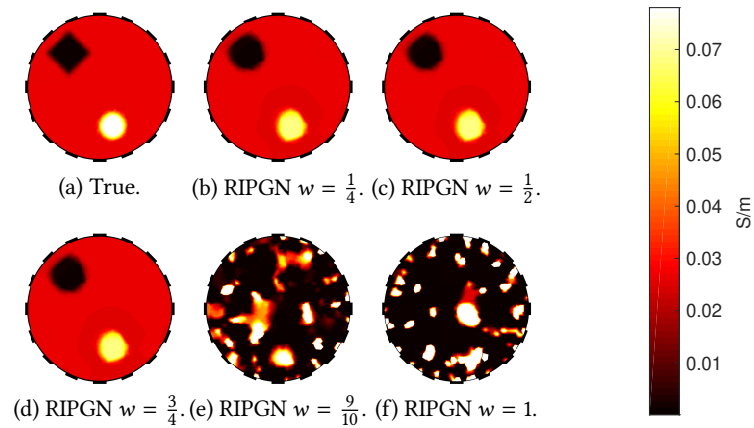


Figure 18: Case 8. True conductivity (a), RIPGN-based reconstructions corresponding to five relaxation parameters w (b)–(f).

Table 9: Case 5. The number of iterations required for convergence, value of the objective function at the last iterate, computational time, and relative error of the estimate for the RIPGN.

Algorithm	Iterations (K)	$J(\hat{\sigma})$	Time (s)	RE(%)
RIPGN $w = 1/4$	34	69.493	1025.7	8.6152
RIPGN $w = 1/2$	16	70.155	498.23	8.6516
RIPGN $w = 3/4$	12	69.57	367.28	8.6591
RIPGN $w = 9/10$	8	$5.2339 \cdot 10^8$	234.4	157.91
RIPGN $w = 1$	8	$6.6964 \cdot 10^8$	239.45	346.57

APPENDIX B.O.1 CASES 9 & 10: WATER TANK EXPERIMENTS

In Cases 9–10, we evaluate RIPGN with experimental data, using a water tank, the geometry of which corresponds to Cases 1–3 (and 7–8). The same objective function (Scheme 3; Section 4.2.3) and parameters chosen in Cases 3 and 8 are used in these reconstructions. All reconstructions are computed with relaxation parameter $w = 3/4$.

Reconstructions in Cases 9–10 are shown in Figure 19. In both cases, the plastic inclusions appear as areas of low conductivity, and in Case 10, the metal inclusion causes an area of increased conductivity. These areas are able to capture the locations of the inclusions well and are easily distinguished from the background as the conductivities of the background and these areas are flat and sharp-edged. The background conductivity in both cases is between 0.02 S/m and 0.03 S/m, which is in the range of typical drinking water in room temperatures, and as expected, the conductivity near the plastic inclusion is very low compared to the background. However, there is some contrast loss in the conductivity around the metal inclusion in Case 10; the conductivity in this region is only about twice as much as the background (see Section 5.2.4). Furthermore, in both cases, the shapes of the inclusions are slightly distorted. This kind of distortion can be caused by a small discrepancy between the geometry of the mesh and the actual measurement setup and other modeling errors. The roundness of the objects could be reinforced by, for example, increasing the value of the regularization parameter α , but the parameter selection for the regularization is beyond the scope of this paper.

The results of the water tank experiments (Cases 9–10) confirm that the RIPGN method proposed in this paper is applicable to EIT imaging also with real measurement data.

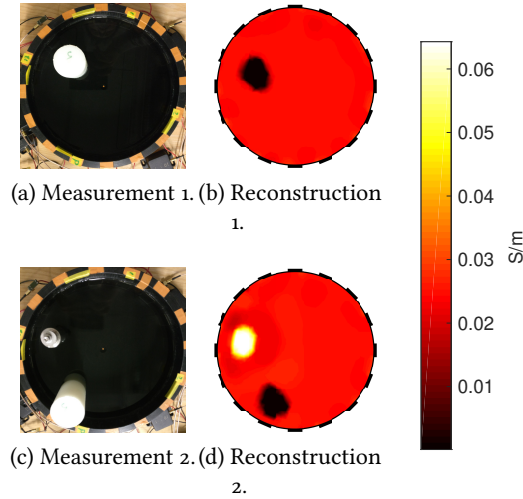


Figure 19: Case 9 (top row) and Case 10 (bottom row). Photos of the measurement setup (left column) and the TV-based RIPGN-reconstructions with $w = 3/4$.

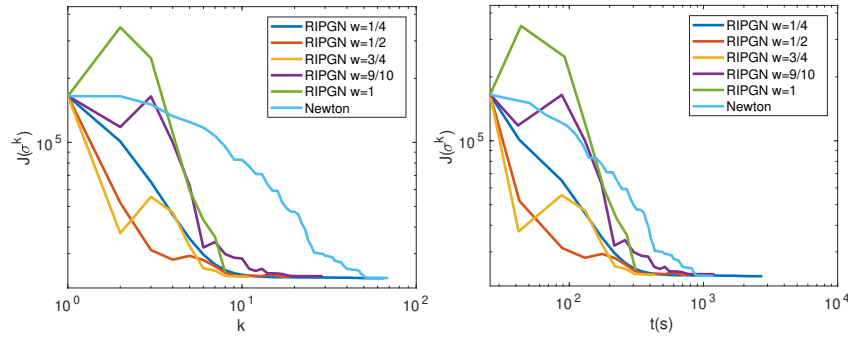


Figure 20: Case 11. Value of the objective function J as function of iteration number k (left), and computational time t (right) for the RIPGN and Newton's method.

APPENDIX B.O.2 CASES 11 & 12: SENSING SKIN EXPERIMENTS

Case 11 is complementary to Case 4; the measurements are done using the same sensing skin setup and computations use the same scheme (Scheme 3). An additional crack was made on the sensing for this measurement. Figure 21 (top left) shows a photograph of the sensing skin in Case 11. The results from this dataset are shown in Figures 20–21 and in Table 10. In this case, RIPGN with relaxation parameter $w = 1/4$ converges better than with the other relaxation parameters, including $w = 1/2$. Although the convergence is better with $w = 1/4$, Figure 21 shows that impact of the relaxation parameter on the reconstruction quality is still fairly negligible. Contrarily, Figure 20 and Table 10 show that, again, the relaxation parameter heavily affects the computation times.

Case 12 is complementary to Case 5; it uses Scheme 3 and the same measurements as in Case

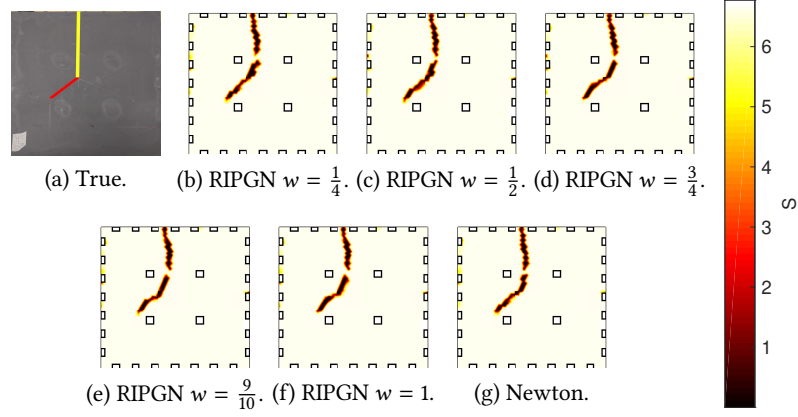


Figure 21: Case 11. Photo of the sensing skin (crack highlighted) (a), RIPGN-based reconstructions corresponding to five relaxation parameters w (b)–(f), and the Newton-based reconstruction (g).

Table 10: Case 11. The number of iterations required for convergence, value of the objective function at the last iterate, and computational time for the RIPGN and the Newton's method.

Algorithm	Iterations (K)	$J(\hat{\sigma})$	Time (s)
RIPGN $w = 1/4$	65	23011	2747.8
RIPGN $w = 1/2$	19	23262	775.53
RIPGN $w = 3/4$	11	23365	436.94
RIPGN $w = 9/10$	29	23533	1206.2
RIPGN $w = 1$	8	24544	311.8
Newton	69	23072	1188.2

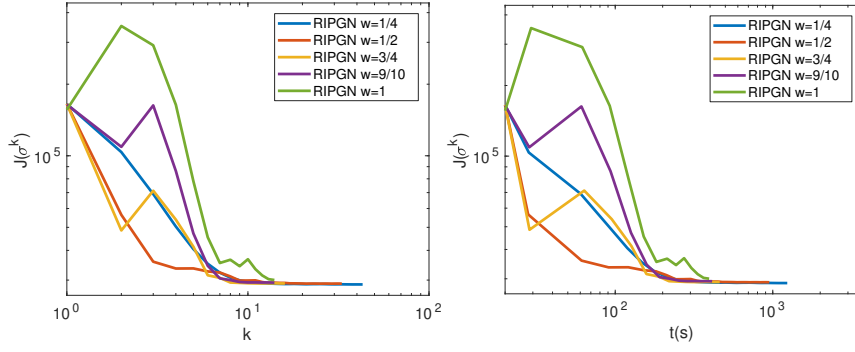


Figure 22: Case 12. Value of the objective function J as function of iteration number k (left), and computational time t (right) for the RIPGN.

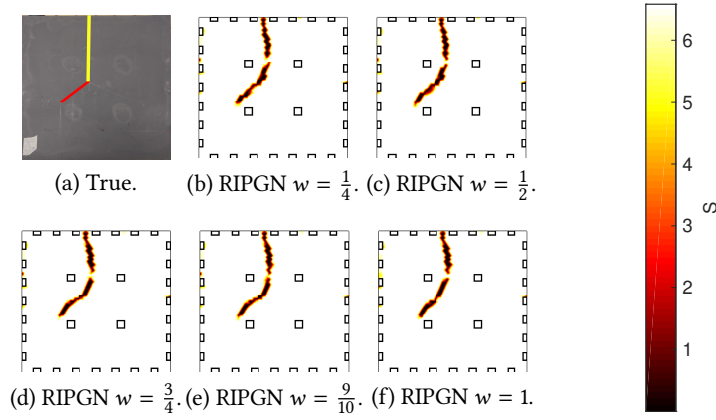


Figure 23: Case 12. Photo of the sensing skin (crack highlighted) (a), RIPGN-based reconstructions corresponding to five relaxation parameters w (b)–(f).

Table 11: Case 12. The number of iterations required for convergence, value of the objective function at the last iterate, and computational time for the RIPGN and the Newton's method.

Algorithm	Iterations (K)	$J(\hat{\sigma})$	Time (s)
RIPGN $w = 1/4$	43	28761	1235.8
RIPGN $w = 1/2$	33	28984	950.35
RIPGN $w = 3/4$	16	29042	460.37
RIPGN $w = 9/10$	14	29280	412.17
RIPGN $w = 1$	14	30021	394.34

11. Results in Case 11, in are shown in [Figure 22–23](#) and [Table 11](#). Differences between Case 11 and Case 12 are fairly similar to differences between Case 4 and 5.

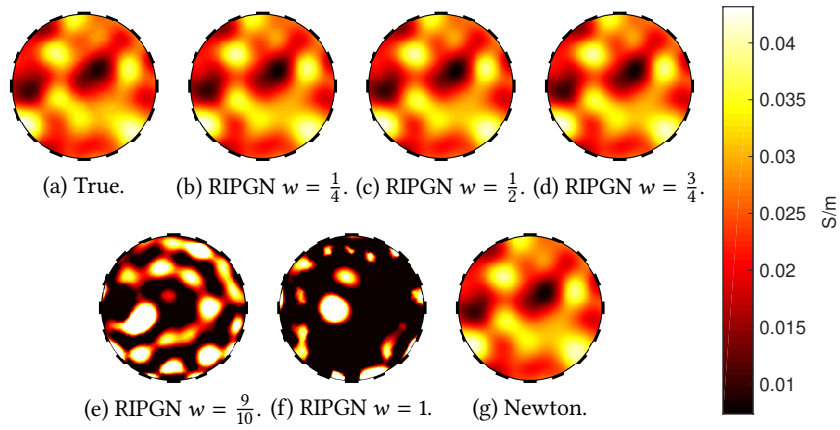


Figure 24: Case 1. True conductivity (a), RIPGN-based reconstructions corresponding to five relaxation parameters w (b)–(f), and the Newton-based reconstruction (g).

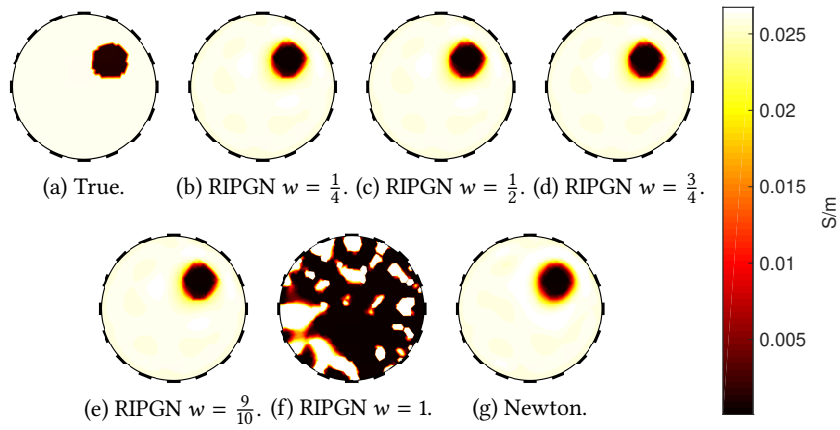


Figure 25: Case 2. True conductivity (a), RIPGN-based reconstructions corresponding to five relaxation parameters w (b)–(f), and the Newton-based reconstruction (g).

APPENDIX C ADDITIONAL RECONSTRUCTIONS IN CASES 1–6

Figures 24–29 show all reconstruction images computed in Cases 1–6, respectively.

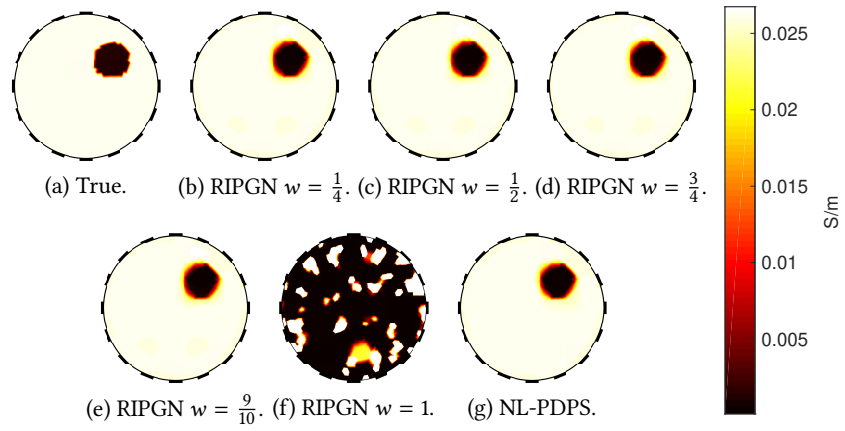


Figure 26: Case 4. True conductivity (a), RIPGN-based reconstructions corresponding to five relaxation parameters w (b)–(f), and the NL-PDPS-based reconstruction (g).

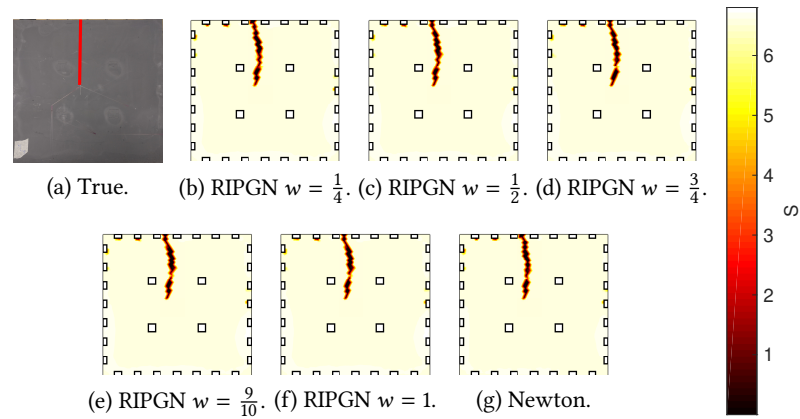


Figure 27: Case 4. Photo of the sensing skin (crack highlighted) (a), RIPGN-based reconstructions corresponding to five relaxation parameters w (b)–(f), and the Newton-based reconstruction (g).

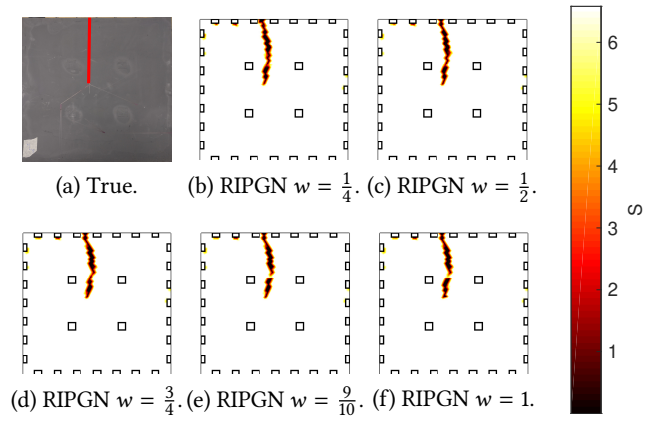


Figure 28: Case 5. Photo of the sensing skin (crack highlighted) (a), RIPGN-based reconstructions corresponding to five relaxation parameters w (b)–(f).

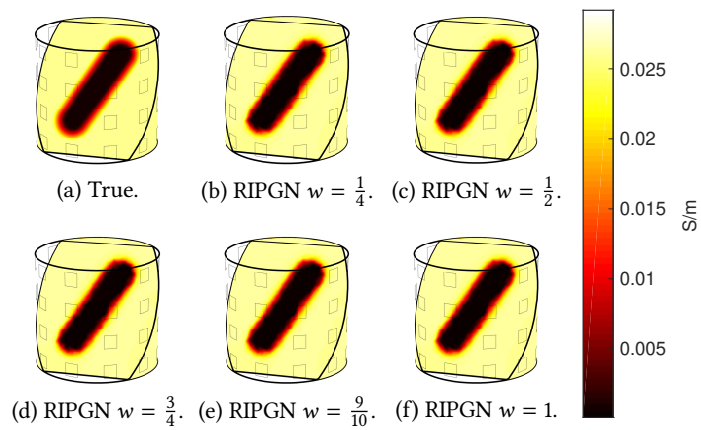


Figure 29: Case 6. True conductivity (a), RIPGN-based reconstructions corresponding to five relaxation parameters w (b)–(f). A tomographic slice of the distribution along plane $p(x) = -x_1 - x_2 + x_3 = 14$ is shown in the figures.

APPENDIX D COMPLEMENTARY PROXIMAL MAPPINGS

Table 12 collects the proximal mappings required in the algorithm implementations.

Table 12: Proximal mappings of G utilized in the algorithm implementations. For the hypercube V , $\text{proj}_{[V_{\min}, V_{\max}]}(x_i) = \max(\min(x_i, V_{\max}), V_{\min})$.

$G(x)$	i 'th component of $\text{prox}_{tG}(x)$
0	x_i
$\delta_V(x)$	$\text{proj}_V(x_i)$
$\delta_V(x) + \frac{\beta}{2}\ x - z^k\ ^2$	$\text{proj}_V\left(\frac{\frac{1}{t}x_i + \beta z_i^k}{\frac{1}{t} + \beta}\right)$
$\delta_V(x) + \frac{\beta}{2}\ x - z^k\ ^2 + B_{\min}(x) + B_{\max}(x)$	$\begin{cases} \text{proj}_V\left(\frac{l_{\min}^2 z_{\min} + \frac{1}{t}x_i + \beta z_i^k}{l_{\min}^2 + \frac{1}{t} + \beta}\right), & x_i < z_{\min} \\ \text{proj}_V\left(\frac{\frac{1}{t}x_i + \beta z_i^k}{\frac{1}{t} + \beta}\right), & z_{\min} \leq x_i \leq z_{\max} \\ \text{proj}_V\left(\frac{l_{\max}^2 z_{\max} + \frac{1}{t}x_i + \beta z_i^k}{l_{\max}^2 + \frac{1}{t} + \beta}\right), & x_i > z_{\max} \end{cases}$

APPENDIX E DETAILS ON THE COMPUTATION OF THE JACOBIAN

The Jacobian $\nabla I(\sigma^k)^*$ can be constructed from the partial derivatives we described briefly in Section 4.1,

$$(E.1) \quad \frac{\partial I^P(\sigma^k)}{\partial \sigma_i} = -\mathcal{K}D(\sigma^k)^{-1} \frac{\partial D(\sigma^k)}{\partial \sigma_i} \theta^P(\sigma^k),$$

where we highlighted that $I^P = I^P(\sigma_1, \dots, \sigma_N)$, $D = D(\sigma_1, \dots, \sigma_N)$, and $\theta^P = \theta^P(\sigma_1, \dots, \sigma_N)$ depend on the iteration through σ^k . Note that θ^P can be obtained by solving the forward problem (4.2). Furthermore, $x^* := \mathcal{K}D(\sigma^k)^{-1}$, can be solved from the linear system $D(\sigma^k)^*x = \mathcal{K}^*$, similarly to the forward problem. Also note that D , as defined in (4.2), is linear in σ , so the term $\frac{\partial D(\sigma^k)}{\partial \sigma_i}$ is independent of the iteration and can be preconstructed. Note that the matrix $\frac{\partial D(\sigma^k)}{\partial \sigma_i} \in \mathbb{R}^{(N+L-1) \times (N+L-1)}$, is very sparse: if the degree of the node i in the FEM grid is n , then this matrix has maximum of $(n+1)^2$ non-zero elements. Instead of storing it as a compressed sparse column (CSC) matrix, we store it as a dense $(n+1) \times (n+1)$ matrix together with indexing arrays to extract the relevant components of $\mathcal{K}D(\sigma^k)^{-1}$ and $\theta^P(\sigma^k)$ to compute the product in (E.1). This product can be computed very cheaply and fully in parallel over the nodes i . Due to the substantial reduction in indexing, this approach in practise significantly improves the computational time of the Jacobian compared to CSC matrices. Finally, the i :th column of Jacobian matrix is $\frac{\partial I}{\partial \sigma_i} = \left(\frac{\partial I^1}{\partial \sigma_i}, \dots, \frac{\partial I^L}{\partial \sigma_i}\right)$.

REFERENCES

- [1] F. J. Aragón Artacho and M. H. Geoffroy, Characterization of metric regularity of subdifferentials, *Journal of Convex Analysis* 15 (2008), 365–380.
- [2] K. Astala and L. Päivärinta, Calderón’s inverse conductivity problem in the plane, *Annals of Mathematics* (2006), 265–299.
- [3] H. Attouch, J. Bolte, and B. Svaiter, Convergence of descent methods for semi-algebraic and tame problems: proximal algorithms, forward–backward splitting, and regularized Gauss–Seidel methods, *Mathematical Programming* 137 (2013), 91–129, [doi:10.1007/s10107-011-0484-9](https://doi.org/10.1007/s10107-011-0484-9).
- [4] J. M. Bardsley, A. Seppänen, A. Solonen, H. Haario, and J. Kaipio, Randomize-then-optimize for sampling and uncertainty quantification in electrical impedance tomography, *SIAM/ASA Journal on Uncertainty Quantification* 3 (2015), 1136–1158.
- [5] A. Beck, *First-Order Methods in Optimization*, SIAM, Philadelphia, PA, 2017, [doi:10.1137/1.9781611974997](https://doi.org/10.1137/1.9781611974997).
- [6] J. Bolte, S. Sabach, and M. Teboulle, Nonconvex Lagrangian-based optimization: monitoring schemes and global convergence, *Mathematics of Operations Research* 43 (2018), 1051–1404, [doi:10.1287/moor.2017.0900](https://doi.org/10.1287/moor.2017.0900).
- [7] J. V. Burke and M. C. Ferris, A Gauss–Newton method for convex composite optimization, *Mathematical Programming* 71 (1995), 179–194, [doi:10.1007/bf01585997](https://doi.org/10.1007/bf01585997).
- [8] A. P. Calderón, On an inverse boundary value problem, *Computational & Applied Mathematics* 25 (2006), 133–138.
- [9] A. Chambolle and T. Pock, A first-order primal-dual algorithm for convex problems with applications to imaging, *Journal of Mathematical Imaging and Vision* 40 (2011), 120–145, [doi:10.1007/s10851-010-0251-1](https://doi.org/10.1007/s10851-010-0251-1).
- [10] K. S. Cheng, D. Isaacson, J. Newell, and D. G. Gisser, Electrode models for electric current computed tomography, *IEEE Transactions on Biomedical Engineering* 36 (1989), 918–924.
- [11] F. Clarke, *Optimization and Nonsmooth Analysis*, Society for Industrial and Applied Mathematics, 1990, [doi:10.1137/1.9781611971309](https://doi.org/10.1137/1.9781611971309).
- [12] C. Clason, S. Mazurenko, and T. Valkonen, Acceleration and global convergence of a first-order primal–dual method for nonconvex problems, *SIAM Journal on Optimization* 29 (2019), 933–963, [doi:10.1137/18m1170194](https://doi.org/10.1137/18m1170194).
- [13] T. A. Davis, Algorithm 832: UMFPACK V4.3—an Unsymmetric-pattern Multifrontal Method, *ACM Trans. Math. Softw.* 30 (2004), 196–199, [doi:10.1145/992200.992206](https://doi.org/10.1145/992200.992206), <http://doi.acm.org/10.1145/992200.992206>.
- [14] M. H. DeGroot, *Optimal statistical decisions*, volume 82, John Wiley & Sons, 2005.

- [15] O. Ferreira, M. Gonçalves, and P. Oliveira, Convergence of the Gauss–Newton Method for Convex Composite Optimization under a Majorant Condition, *SIAM Journal on Optimization* 23 (2013), 1757–1783, [doi:10.1137/110841606](https://doi.org/10.1137/110841606).
- [16] G. Garrigos, L. Rosasco, and S. Villa, Convergence of the forward-backward algorithm: Beyond the worst case with the help of geometry (2017).
- [17] G. González, V. Kolehmainen, and A. Seppänen, Isotropic and anisotropic total variation regularization in electrical impedance tomography, *Computers & Mathematics with Applications* 74 (2017), 564–576.
- [18] M. Hallaji, A. Seppänen, and M. Pour-Ghaz, Electrical impedance tomography-based sensing skin for quantitative imaging of damage in concrete, *Smart Materials and Structures* 23 (2014), 085001, [doi:10.1088/0964-1726/23/8/085001](https://doi.org/10.1088/0964-1726/23/8/085001), <https://doi.org/10.1088/0964-1726/23/8/085001>.
- [19] M. Hanke, A regularizing Levenberg-Marquardt scheme, with applications to inverse groundwater filtration problems, *Inverse Problems* 13 (1997), 79, [doi:10.1088/0266-5611/13/1/007](https://doi.org/10.1088/0266-5611/13/1/007).
- [20] J. B. Hiriart-Urruty and C. Lemaréchal, *Fundamentals of Convex Analysis*, Springer, 2001, [doi:10.1007/978-3-642-56468-0](https://doi.org/10.1007/978-3-642-56468-0).
- [21] J. Kaipio and E. Somersalo, *Statistical and computational inverse problems*, volume 160, Springer Science & Business Media, 2006.
- [22] B. Kaltenbacher, A. Neubauer, and O. Scherzer, *Iterative Regularization Methods for Non-linear Ill-Posed Problems*, number 6 in Radon Series on Computational and Applied Mathematics, De Gruyter, 2008.
- [23] R. Kohn and M. Vogelius, Determining conductivity by boundary measurements, *Communications on Pure and Applied Mathematics* 37 (1984), 289–298.
- [24] R. V. Kohn and M. Vogelius, Determining conductivity by boundary measurements II. Interior results, *Communications on Pure and Applied Mathematics* 38 (1985), 643–667.
- [25] A. S. Lewis, Active Sets, Nonsmoothness, and Sensitivity, *SIAM Journal on Optimization* 13 (2002), 702–725, [doi:10.1137/s1052623401387623](https://doi.org/10.1137/s1052623401387623).
- [26] A. S. Lewis and S. Zhang, Partial Smoothness, Tilt Stability, and Generalized Hessians, *SIAM Journal on Optimization* 23 (2013), 74–94, [doi:10.1137/110852103](https://doi.org/10.1137/110852103).
- [27] C. Li and X. Wang, On convergence of the Gauss-Newton method for convex composite optimization, *Mathematical Programming* 91 (2002), 349–356, [doi:10.1007/s101070100249](https://doi.org/10.1007/s101070100249).
- [28] J. Liang, J. Fadili, and G. Peyré, Local Linear Convergence of Forward–Backward under Partial Smoothness, *Advances in Neural Information Processing Systems* 27 (2014), 1970–1978, <http://papers.nips.cc/paper/5260-local-linear-convergence-of-forward-backward-under-partial-smoothness.pdf>.

- [29] A. Lipponen, A. Seppanen, and J. P. Kaipio, Electrical impedance tomography imaging with reduced-order model based on proper orthogonal decomposition, *Journal of Electronic Imaging* 22 (2013), 023008.
- [30] S. Mazurenko, J. Jauhiainen, and T. Valkonen, Primal-dual block-proximal splitting for a class of non-convex problems, 2019, [arXiv:1911.06284](https://arxiv.org/abs/1911.06284). submitted.
- [31] R. Mifflin, Semismooth and semiconvex functions in constrained optimization, *SIAM Journal on Control And Optimization* 15 (1977), 959–972, [doi:10.1137/0315061](https://doi.org/10.1137/0315061).
- [32] J.L. Mueller and S. Siltanen, *Linear and Nonlinear Inverse Problems with Practical Applications*, SIAM, 2012, [doi:10.1137/1.9781611972344](https://doi.org/10.1137/1.9781611972344).
- [33] J. Nocedal and S. Wright, *Numerical Optimization*, Springer Series in Operations Research and Financial Engineering, Springer New York, 2006, [doi:10.1007/978-0-387-40065-5](https://doi.org/10.1007/978-0-387-40065-5).
- [34] J. Pang and L. Qi, Nonsmooth Equations: Motivation and Algorithms, *SIAM Journal on Optimization* 3 (1993), 443–465, [doi:10.1137/0803021](https://doi.org/10.1137/0803021).
- [35] T. Pock and A. Chambolle, Diagonal preconditioning for first order primal-dual algorithms in convex optimization, in *Computer Vision (ICCV), 2011 IEEE International Conference on*, 2011, 1762–1769, [doi:10.1109/iccv.2011.6126441](https://doi.org/10.1109/iccv.2011.6126441).
- [36] L. Q. Qi, Convergence analysis of some algorithms for solving nonsmooth equations, *Math. Oper. Res.* 18 (1993), 227–244, [doi:10.1287/moor.18.1.227](https://doi.org/10.1287/moor.18.1.227).
- [37] L. Q. Qi and J. Sun, A nonsmooth version of Newton’s method, *Mathematical Programming* 58 (1993), 353–367, [doi:10.1007/bf01581275](https://doi.org/10.1007/bf01581275).
- [38] L. I. Rudin, S. Osher, and E. Fatemi, Nonlinear total variation based noise removal algorithms, *Physica D: nonlinear phenomena* 60 (1992), 259–268.
- [39] M. Salo, Calderón problem, *Lecture Notes* (2008).
- [40] S. Salzo and S. Villa, Convergence analysis of a proximal Gauss-Newton method, *Computational Optimization and Applications* 53 (2012), 557–589, [doi:10.1007/s10589-012-9476-9](https://doi.org/10.1007/s10589-012-9476-9).
- [41] E. Somersalo, M. Cheney, and D. Isaacson, Existence and uniqueness for electrode models for electric current computed tomography, *SIAM Journal on Applied Mathematics* 52 (1992), 1023–1040.
- [42] J. Sylvester and G. Uhlmann, A global uniqueness theorem for an inverse boundary value problem, *Annals of mathematics* (1987), 153–169.
- [43] G. Uhlmann, Electrical impedance tomography and Calderón’s problem, *Inverse Problems* 25 (2009), 123011, [doi:10.1088/0266-5611/25/12/123011](https://doi.org/10.1088/0266-5611/25/12/123011).
- [44] T. Valkonen, A primal-dual hybrid gradient method for non-linear operators with applications to MRI, *Inverse Problems* 30 (2014), 055012, [doi:10.1088/0266-5611/30/5/055012](https://doi.org/10.1088/0266-5611/30/5/055012).

- [45] T. Valkonen, Preconditioned proximal point methods and notions of partial subregularity, 2017. Submitted.
- [46] T. Valkonen, Block-proximal methods with spatially adapted acceleration, *Electronic Transactions on Numerical Analysis* 51 (2019), 15–49, [doi:10.1553/etna_vol51s15](https://doi.org/10.1553/etna_vol51s15).
- [47] T. Valkonen, First-order primal-dual methods for nonsmooth nonconvex optimisation, 2019, [arXiv:1910.00115](https://arxiv.org/abs/1910.00115). submitted.
- [48] P. J. Vauhkonen, *Image reconstruction in three-dimensional electrical impedance tomography*, Kuopion yliopisto, 2004.
- [49] A. Voss, *Imaging moisture flows in cement-based materials using electrical capacitance tomography*, PhD thesis, University of Eastern Finland, 2020.